Analysis of hydrogen-powered propulsion system alternatives for diesel-electric regional trains

Kapetanović, Marko ; Nunez, Alfredo; van Oort, Niels; Goverde, Rob M.P.

Important note
To cite this publication, please use the final published version (if applicable).
Please check the document version above.

Analysis of hydrogen-powered propulsion system alternatives for diesel-electric regional trains

Marko Kapetanović [a],[*], Alfredo Núñez [b], Niels van Oort [a], Rob M.P. Goverde [a]

[a] *Department of Transport and Planning, Delft University of Technology, P.O. Box 5048, 2600, GA, Delft, the Netherlands*
[b] *Section of Railway Engineering, Delft University of Technology, P.O. Box 5048, 2600, GA, Delft, the Netherlands*

A B S T R A C T

Non-electrified regional railway lines with typically employed diesel-electric multiple units require alternative propulsion systems to meet increasingly strict emissions regulations. With the aim to identify an optimal alternative to conventional diesel traction, this paper presents a model-based assessment of hydrogen-powered propulsion systems with an internal combustion engine or fuel cells as the prime mover, combined with different energy storage system configurations, based on lithium-ion batteries and/or double-layer capacitors. The analysis encompasses technology identification, design, modelling and assessment of alternative powertrains, explicitly considering case-related constraints imposed by the infrastructure, technical and operational requirements. Using a regional railway network in the Netherlands as a case, we investigate the possibilities in converting a conventional benchmark vehicle and provide the railway undertaking and decision-makers with valuable input for planning of future rolling stock investments. The results indicate the highest fuel-saving potential for fuel cell-based hybrid propulsion systems with lithium-ion battery or a hybrid energy storage system that combines both energy storage system technologies. The two configurations also demonstrate the highest reduction of greenhouse gas emissions compared to the benchmark diesel-driven vehicle, by about 25% for hydrogen produced by steam methane reforming, and about 19% for hydrogen obtained from electrolysis of water with grey electricity.

1. Introduction

Regional non-electrified railway networks require the identification of alternative traction options to meet strict regulations and emission reduction targets imposed on the railway sector (Beatrice et al., 2013; UIC and CER, 2012). Hydrogen-based vehicle technologies are a potentially suitable alternative to typically employed diesel-electric multiple units (DEMU) in regional passenger transport (Klebsch et al., 2020). Fuel cells (FC) are a dominant technology for onboard power generation in hydrogen-related railway applications. FCs offer numerous advantages compared to internal combustion engines (ICE), summoned primarily in high efficiency, quiet and emission-free operations at the point of use, with water vapor and heat as the only products (Sun et al., 2021). However, their main drawback is the slow dynamic response, which requires vehicle hybridization with an energy storage system (ESS) and accompanying energy management and control strategy (EMCS), which would cover power fluctuations and allow for the recuperation

---

Nomenclature

Abbreviations

AC	alternating current
AFC	alkaline fuel cell
CO_2	carbon dioxide
DC	direct current
DEMU	diesel-electric multiple unit
DLC	double-layer capacitor
EGU	engine-generator unit
EMCS	energy management and control strategy
ESS	energy storage system
FC	fuel cell
FCMU	fuel cell multiple unit
FSM	finite state machine
GHG	greenhouse gasses
GTW	Gelenktriebwagen
HESS	hybrid energy storage system
HVAC	heating, ventilation and air conditioning
ICE	internal combustion engine
IGBT	insulated-gate bipolar transistor
LB	lithium-ion battery
LHV	low heating value
LSC	lanthanum strontium cobaltite
LTO	lithium titanium oxide
MCFC	molten carbonate fuel cell
NMC	nickel manganese cobalt
NO_x	nitrogen oxides
OB	optimization-based
PAFC	phosphoric acid fuel cell
PEMFC	polymer electrolyte membrane (proton-exchange membrane) fuel cell
PLR	part load ratio
SoC	state-of-charge
SOFC	solid oxide fuel cell

Parameters

C_{DLC}	capacitance of the double-layer capacitor [F]
d_w	wheel diameter [m]
g	gravitational acceleration $[m/s^2]$
i_{ag}	constant gear ratio $[-]$
$I_{DLC}^{max,ch}$	allowed maximum charging current for the double-layer capacitor [A]
$I_{DLC}^{max,dch}$	allowed maximum discharging current for the double-layer capacitor [A]
$I_{LB}^{cont,ch}$	allowed maximum continuous charging current of the battery [A]
$I_{LB}^{cont,dch}$	allowed maximum continuous discharging current of the battery [A]
$I_{LB}^{peak,ch}$	allowed peak (pulse) charging current of the battery [A]
$I_{LB}^{peak,dch}$	allowed peak (pulse) discharging current of the battery [A]
m_{pax}	total weight of passengers [kg]
m_{tare}	empty vehicle mass [kg]
m_v	total vehicle mass [kg]
$P_{aux,const}$	constant auxiliaries power [W]
p_{cool}	cooling power coefficient $[-]$
P_{FC}^{idle}	idling power load for the fuel cell [W]
P_{FC}^{rated}	rated power of the fuel cell [W]
P_{FC}^{opt}	optimal level of electrical power from the fuel cell [W]
P_G^{idle}	idling power load for the engine-generator unit [W]
P_G^{max}	maximum power load for the engine-generator unit [W]
P_G^{min}	minimum power load for the engine-generator unit [W]
P_G^{opt}	optimal level of electrical power from the engine-generator unit [W]

Q_{LB}　nominal capacity of the battery [As]

R_{DLC}　internal resistance of the double-layer capacitor [Ω]

R_{LB}^{ch}　battery internal resistance during charge [Ω]

R_{LB}^{dch}　battery internal resistance during discharge [Ω]

r_0　Davis equation coefficient (constant term) [N]

r_1　Davis equation coefficient (linear term) [N/(m/s)]

r_2　Davis equation coefficient (quadratic term) $\left[\text{N/(m/s)}^2\right]$

t_{peak}^{ch}　time limit for the allowed battery pulse charging current [s]

t_{peak}^{dch}　time limit for the allowed battery pulse discharging current [s]

U_{DLC}^{max}　maximum voltage of the double-layer capacitor [V]

U_{DLC}^{min}　minimum voltage of the double-layer capacitor [V]

U_{LB}^{max}　maximum battery voltage [V]

U_{LB}^{min}　minimum battery voltage [V]

v_{max}　maximum velocity [m/s]

Δt　simulation (integration) time step [s]

η_{ag}　constant efficiency of the gearbox [−]

λ　rotating mass factor [−]

σ_{DLC}^{max}　maximum state-of-charge for double-layer capacitor [−]

σ_{DLC}^{min}　minimum state-of-charge for double-layer capacitor [−]

σ_{ESS}^{hyst}　energy storage system hysteresis cycle limit for the state-of-charge [−]

σ_{ESS}^{lim}　state-of-charge limit for the energy storage system [−]

σ_{ESS}^{max}　maximum state-of-charge for the energy storage system [−]

σ_{ESS}^{min}　minimum state-of-charge for the energy storage system [−]

σ_{LB}^{max}　maximum battery state-of-charge [−]

σ_{LB}^{min}　minimum battery state-of-charge [−]

Dynamic variables

a　vehicle acceleration $\left[\text{m/s}^2\right]$

$Flag$　binary indicator for the state-of-charge hysteresis cycle [−]

F_w　tractive/braking effort at the wheel [N]

I_{DLC}　current of the double-layer capacitor [A]

I_{DLC}^{max}　maximum current of the double-layer capacitor [A]

I_{DLC}^{min}　minimum current of the double-layer capacitor [A]

I_{LB}　battery current [A]

I_{LB}^{max}　maximum battery current [A]

$I_{LB}^{max,ch}$　maximum battery charging current defined by the manufacturer [A]

$I_{LB}^{max,dch}$　maximum battery discharging current defined by the manufacturer [A]

I_{LB}^{min}　minimum battery current [A]

m_{FC}　instantaneous fuel consumption of fuel cell [kg/s]

m_{ICE}　instantaneous fuel consumption of internal combustion engine [kg/s]

M_{FC}　cumulative fuel consumption of fuel cell [kg]

M_{ICE}　cumulative fuel consumption internal combustion engine [kg]

P_{aux}　total auxiliaries power [W]

P_{dem}　total requested power for traction and auxiliaries [W]

P_{DLC}　power of the double-layer capacitor [W]

P_{DLC}^{max}　maximum power of the double-layer capacitor [W]

P_{DLC}^{min}　minimum power of the double-layer capacitor [W]

P_{EM}　electric power of the electric motor [W]

P_{FC}　electrical output power of the fuel cell [W]

P_{FC}^{max}　maximum power of the fuel cell [W]

P_{FC}^{min}　minimum power of the fuel cell [W]

P_G　electrical output power of the generator [W]

P_{ICE}　mechanical output power of the internal combustion engine [W]

P_{LB}　power of the battery [W]

P_{LB}^{max}　maximum power of the battery [W]

P_{LB}^{min}　minimum power of the battery [W]

R_c　curve resistances [N]

R_g　grade resistances [N]

R_{LB}	battery internal resistance [Ω]	
R_v	vehicle resistances [N]	
s	distance travelled [m]	
t	time [s]	
t_{cnt}^{ch}	battery pulse charging time counter [s]	
t_{cnt}^{dch}	battery pulse discharging time counter [s]	
T_{EM}	torque at the mechanical output of the electric motor [Nm]	
T_w	torque at the wheel [Nm]	
U_{DLC}	terminal voltage of the double-layer capacitor [V]	
U_{LB}	battery terminal voltage [V]	
U_{OC}	battery open circuit voltage [V]	
v	vehicle velocity [m/s]	
γ	angle of the slope [rad]	
η_{EM}	efficiency of the electric motor [−]	
η_{FC}	efficiency of the fuel cell [−]	
η_{G}	efficiency of the generator [−]	
σ_{DLC}	state-of-charge of the double-layer capacitor [−]	
σ_{LB}	battery state-of-charge [−]	
φ	curve radius [m]	
ψ	specific fuel consumption [kg/Ws]	
ω_{EM}	rotational speed of the electric motor [rad/s]	
ω_{ICE}	rotational speed of the internal combustion engine [rad/s]	
ω_w	rotational speed of the wheel [rad/s]	

of braking energy (Siddiqui and Dincer, 2019).

Following rapid technology developments and availability of FC technologies, several fuel cell multiple units (FCMU) have been introduced in the market by some of the major railway vehicle manufacturers, e.g., Coradia iLint from Alstom (2020), Mireo Plus H from Siemens (FuelCellWorks, 2020), and Stadler's Zillertalbahn narrow-gauge FCMU (IRJ, 2019). Furthermore, considering the service life of railway vehicles, typically spanning over 30 years, it could be advantageous to convert existing vehicles to their hydrogen-powered counterparts instead of replacing them with new commercially available alternatives. A prominent recent example for the regional train is UK's train HydroFLEX, in operation since 2019 (Calvert et al., 2021; Gallucci, 2019).

Although MAN produces hydrogen ICEs for busses (Knorr et al., 1998; MAN, 2020), no commercial railway vehicles are powered by a hydrogen ICE. However, another major ICE manufacturer Deutz recently announced the introduction of hydrogen ICEs in 2024, aimed at railway applications (Deutz, 2021). Hydrogen combustion in ICE does not produce greenhouse gas (GHG) emissions; however, local pollutants such as nitrogen oxides (NO$_x$) are emitted due to high-temperature hydrogen combustion with air. Their main advantage is that they are based on well-established technology, as they mostly represent modifications of existing ICEs running on compressed natural gas (Akal et al., 2020), and have a service life three times longer than the FCs (Marin et al., 2010). Based on the previous experience with other technologies that found their place in railway applications, as a result of spillovers from other modes of transport such as busses and passenger cars, together with the relatively low price compared to the emerging technology as FCs, hydrogen ICEs could be considered as a carbon-neutral bridging solution towards totally-emission free railway transport.

The transition from conventional DEMUs to alternative systems is a complex dynamic decision-making process that involves various stakeholders and multiple aspects to be considered. It requires in-depth analyses that include identification of available technology, design, modelling, and assessment of potential alternatives, with respect to the particular case-related constraints imposed by infrastructure, technical and operational constraints (e.g., track geometry, speed, and axle load limitations, implemented onboard power control of different power sources, maintaining existing timetables, etc.) (Kapetanović et al., 2021a). Our current study aims to support the design of hydrogen-powered propulsion systems by converting conventional DEMUs, and to present the comparative model-based assessment of different powertrain configurations in terms of overall energy consumption and produced GHG emissions. This research uses a case of the regional railway network in the Northern Netherlands and passenger services provided by Arriva, the largest regional railway undertaking in the Netherlands. The results of this research can serve as an essential input for decision-makers in the planning of future rolling stock investments and trains operations.

The remainder of the paper is organized as follows. A literature review and paper contributions are given in Section 2. Section 3 presents a detailed vehicle simulation model with implemented real-time power-distribution control for identified alternative propulsion systems. The propulsion systems design and a comparative assessment are provided in Section 4. We conclude this paper with a final discussion and future research directions in Section 5.

2. Literature review

Considering the main aim of present study, this section reviews the scientific literature on hydrogen-powered railway vehicles, focusing primarily on a regional passengers' transport context and the four main interrelated aspects: design, modelling, control, and assessment of different propulsion systems.

As noted in the Introduction, FCs are the predominant technology in hydrogen-based propulsion system designs for railway vehicles, which is reflected in extensive literature covering different aspects of their development and deployment. Considering regional passengers transport, various studies analyzed the available commercial FCMUs and the feasibility of their deployment on regional railway networks (Klebsch et al., 2019, 2020; Mueller et al., 2020), using mainly general vehicle characteristics published by the manufacturers (e.g., range, maximum power, etc.), and compared them with the general infrastructure-related requirements for the railway network in question. Although these studies provide rough estimations of FCMUs feasibility and potential benefits, a comprehensive investigation on the available FCMUs would require detailed simulation models coupled with infrastructure and vehicle-specific data, which are often difficult to obtain for the new vehicles. Additionally, field tests and trials (RailTech, 2020) require significant effort and would be a logical next step after completing detailed studies.

With regard to vehicles conversion/retrofit to their hydrogen-powered counterpart, selecting suitable technology is a crucial step in the vehicle powertrain design process. There are several types of FCs, differing in start-up time, efficiency, operating temperature, materials used for their manufacture, costs, etc., with detailed overview and comparison of different FC technologies provided by Bagotsky et al. (2015), Siddiqui and Dincer (2019), and Sun et al. (2021). In general, the polymer electrolyte membrane (or proton-exchange membrane) fuel cell (PEMFC) is the most commonly utilized FC technology, due to numerous advantages over other FC types, reflected in relatively short start-up and shutdown time, and low operating temperature (80 °C). Their main drawbacks are high cost due to the use of expensive metal catalysts, and the platinum catalyst poisoning effect (Carrette et al., 2001; Sopian and Wan Daud, 2006; Wang et al., 2011). The alkaline fuel cell (AFC) is another low-temperature FC technology with lower costs than the PEMFC; however, their sensitivity to CO_2 molecules leads to considerable deterioration of its performance (Kordesch et al., 2000). Phosphoric acid fuel cells (PAFCs) are featured with lower efficiency and higher operating temperature than previous FCs (200 °C), leading to a reduced platinum catalyst poisoning effect and thus longer lifetime (US Department of Energy, 2021). They are mainly employed in stationary power and heat generation systems (Chen et al., 2016). Solid oxide fuel cells (SOFCs) are high-temperature FCs (800–1000 °C), which allows for high power output (up to 2 MW) with high efficiency of 60%, but also causes low performance at lower temperatures, requires long start-up time, higher costs of materials, and sophisticated design and the assembly (Sun et al., 2021). Molten carbonate fuel cells (MCFCs) are another high-temperature FCs (600–650 °C), offering high output power (up to 3 MW), utilized mainly in stationary power generation systems (US Department of Energy, 2021). Considering the applicability to the railway sector, low-temperature PEMFC fits best to non-permanent demand cycles, and applications like light rail vehicles, commuter and regional trains, shunt/switch and underground mine locomotives, while high-temperature SOFC has been seen as a promising technology for freight or heavy haul locomotives, given their long operation time and steady duty cycles (Barbosa, 2019; Sun et al., 2021).

In addition to FCs as the main power source, various ESS technologies have emerged in the transport sector over the last decades, with batteries, double-layer capacitors (DLCs), and flywheels being the most represented solutions depending on the particular application and requirements (Vazquez et al., 2010). Due to their high energy-to-weight ratio, no memory effect, low self-discharge rates, rapid technology development, and commercial availability, lithium-ion batteries (LBs) are the most represented battery and ESS technology in railway applications (Meinert et al., 2015a). DLCs provide high power density and low energy density, making them suitable for peak power shaving and maximizing recuperation of braking energy. They are often coupled with LBs in a hybrid energy storage system (HESS), that combines individual benefits offered by the two technologies (Dittus et al., 2011; Zhang et al., 2019a, 2019b). Flywheels offer fast charging and discharging rates; however, they are featured with various safety issues (González-Gil et al., 2013), high weight and self-discharging rates. Thus, they are not considered in this paper. Detailed characteristics of different ESS technologies are provided in recent reviews by Bagotsky et al. (2015) and Ghaviha et al. (2017).

Comprehensive and reliable mathematical models are required to assess the behavior of system components and to obtain plausible results in terms of energy consumption and efficiency. Models of electrochemical power sources, such as FCs, batteries, and DLCs, can be generally divided into electrochemical models and equivalent electrical circuit models (Zhang et al., 2017). Different dimensions of electrochemical models use electrochemical equations in modelling and describing the distributed electrochemistry reactions in the electrodes and electrolytes. Piraino and Fragiacomo (2020) provided a comprehensive model that incorporates each powertrain component, such as energy sources, power electronics and drivetrain. Although these physics-based models can provide the information on the full dynamic behavior of the system, they require detailed information and numerous parameters on the physical system, which are often difficult to obtain, and employ a set of partial differential equations, which make them too complex for fast simulation purposes (Ghaviha et al., 2019). On the other hand, different orders of equivalent electrical circuit models use different electrical components such as capacitors and resistors to obtain a response similar to the behavior of the physical system (see, Krastev and Tricoli, 2022). They provide high enough accuracy for power management applications, while avoiding unnecessary complexities of the electrochemical models (Fotouhi et al., 2016).

Since the energy management and control strategy (EMCS) is the main driver of the fuel economy for hybrid vehicles, most of the railway literature focuses on this particular aspect, i.e., its development for a particular predefined FCMU powertrain configuration. EMCSs can be generally classified into optimization-based and rule-based strategies, where former are further divided according to the optimization horizon in global optimization, instantaneous optimization, and real-time optimization (Xu et al., 2015). Dynamic programming is a powerful method for solving global optimization problems (as demonstrated by Kapetanović et al., 2021a). Ogawa et al. (2007) proposed an optimal EMCS based on dynamic programming for a FC/DLC railway vehicle, further used in deriving an optimal required capacity for a DLC. The main drawbacks hindering real-time application of dynamic programming are that it requires perfect information on future driving conditions, which is hard to achieve in reality, the long calculation time, and the inability to deal with variables that include counters (see Section 3.2) due to its nature of propagation backward in time. Therefore, these algorithms are often used as a benchmark in developing other causal controls. Tao et al. (2021) combined dynamic programming and state machine control in obtaining optimal power distribution between the FC and DLC for a tram vehicle, demonstrating significant benefits

in terms of fuel economy, efficiency and durability. Regarding regional railway vehicles, Peng et al. (2020b) used dynamic programming in deriving a scalable, causal, adaptive EMCS for an FC/LB powertrain, achieving only 0.01–0.09% increase in fuel consumption compared to the optimal case.

The equivalent consumption minimization and Pontryagin's minimum principle strategies are suitable for instantaneous optimization problems. Torreglosa et al. (2011a) presented an equivalent consumption minimization strategy for an FC/battery hybrid tram, with the results showing significant benefits reflected in fuel savings compared to other causal controls, while at the same time maintaining the battery state-of-charge (SoC). A similar approach is proposed by W. Zhang et al. (2017) in a case of FC/LB/DLC tram. This method is also used as the basis in the development of dynamic power factor control for FC/LB locomotive (Hong et al., 2018). Zhang et al. (2019a, 2019b) proposed a firefly algorithm to optimize the parameters in equivalent consumption minimization strategy for an FC/LB/DLC tram. Liu et al. (2020) employed Pontryagin's minimum principle in defining the optimal EMCS and the optimal braking energy recovery strategy for an FC/DLC tram. Peng et al. (2020a) used the same method as a benchmark in deriving a causal real-time EMCS for a regional railway vehicle. In general, with the future driving conditions properly estimated, the previous two methods can be applied to real-time optimization problems. Some papers propose the use of meta-heuristics for power flows control. Li et al. (2018) employed a genetic algorithm in the case of an FC/LB/DLC low-floor tramcar, with an obtained fuel savings of 15% compared to the baseline rule-based control.

Rule-based strategies are based on event-triggered Boolean or fuzzy rules used in online (real-time) control applications, where rules can be designed according to powertrain characteristics or extracted from optimized algorithms. Garcia et al. (2010) proposed an adaptive rule-based control for a tram by considering eight states in distributing requested power between the FC and a nickel-metal hydride cell battery. A similar control based on a state machine for a hybrid FC/LB tram is proposed by Han et al. (2016). A two-mode multisource coordination EMCS based on self-convergence droop control for a FC/LB/DLC tram is presented by Han et al. (2018). A power-voltage equilibrium strategy based on droop control for an FC/LB/DLC hybrid was proposed by Zhang et al. (2019a, 2019b). Peng et al. (2018) used fuzzy logic in developing a sub-optimal control for an FC/LB/DLC tram by incorporating operational uncertainties, performance degradation and SoC balancing. A fuzzy logic controller for an FC/battery tram based on LB SoC, and FC and traction load was proposed by Torreglosa et al. (2011b). Although rule-based strategies typically cannot offer a proof of optimality, low computation cost and storage memory requirement make them especially suitable for the development of causal real-time controllers, offering at the same time promising benefits in terms of energy consumption reduction (Zhang et al., 2020).

Regarding the powertrain design, several studies reported on a conversion analysis of existing railway vehicles to their hydrogen counterparts. For instance, Washing and Pulugurtha (2016) presented a simulation-based analysis of energy use and emissions for a pure FC and a hybrid FC/LB alternative powertrain for a Siemens light rail vehicle operating in North Carolina. Analyses that employ similar simplified vehicle models are reported for locomotives by Miller et al. (2007) and Peng et al. (2014). Concerning the design of hydrogen-based regional vehicles, a conceptual design of FCMUs, both non-hybrid and hybrid with an LB, is presented by Hoffrichter et al. (2016). The authors investigate the feasibility of converting a standard DEMU from Stadler, by incorporating constraints related to the available weight and volume of the components, as well as the range requirements for the FCMUs. In terms of selection and sizing of powertrain components, the vehicle design is based on a simulated round trip and corresponding energy demand of a standard DEMU, with no detailed models that would capture the dynamics of electrochemical power sources (FC and LB), nor active EMCS implemented. A similar study for the British class 150 regional train is presented by Din and Hillmansen (2018). In contrast to the previous conceptual designs that focus more on the practical implementability of particular technology, while neglecting detailed powertrain and ECMS modelling, some papers employed optimization algorithms that consider the relationship between the EMCS in place and the optimal size of the powertrain components based on selected main criteria and constraints, and focusing mainly on locomotive applications. Such method based on the Krill herd optimization algorithm is presented by Guo et al. (2020) for a hybrid FC/LB locomotive. A Particle Swarm Optimization algorithm combined with several rule-based power controls for a hybrid FC/LB locomotive was presented by Sarma and Ganguly (2020, 2018).

From the literature review it can be noted that an extensive research has been reported on different aspect of hydrogen propulsion systems deployment in the railway sector, focusing mainly on ECMS development for a particular predefined powertrain configuration. However, several limitations and scientific lacks were identified among the prior research. Existing studies focus exclusively on FCs technology, with no reported detailed analyses on hydrogen ICEs, and with only a scarce number of comparative analyses between alternative powertrain configurations and ESS technologies. As a rare example, Hoffrichter et al. (2012) derived the well-to-wheel energy efficiencies and CO_2 emissions for electric, diesel and hydrogen (both pure ICE and pure FC) traction for railway vehicles, using the low and high heating values of the enthalpy of oxidation of the fuel. The theoretical analysis is based on a desk study using typical one-lumped efficiency values found in the literature for individual powertrain components. Furthermore, prior design methods rely mainly on simplified simulation models, neglecting the behavior of individual powertrain components and the influence of the ECMS. It would be advantageous to integrate these aspects together with other significant drivers and physical/safety limitations in a comprehensive powertrain layout design. A recent analysis is provided by Fragiacomo and Piraino (2021) for an innovative vehicle-to-grid FC-based tram application. Regarding the type of vehicle analyzed (market segment), urban railway vehicles (trams) are a predominant category in the literature, followed by locomotives, with a limited number of papers focusing on regional multiple unit railway vehicles. Although the main principles in powertrain design apply to different applications, freight locomotives and trams are characterized with different technical characteristics, stopping patterns, and lower operational speeds, resulting in different energy and power demand, duty cycles, and related design parameters. For instance, Fragiacomo and Piraino (2019) analyzed the use of hydrogen-hybrid powertrains including FCs, LBs and/or DLCs in four different contexts in Southern Italian railways, including detailed powertrain modelling, EMCS, and validation using real-world measurements, with the results indicating a significant impact of case related characteristics on both powertrain design and performance. One of the main challenges in realizing a comprehensive
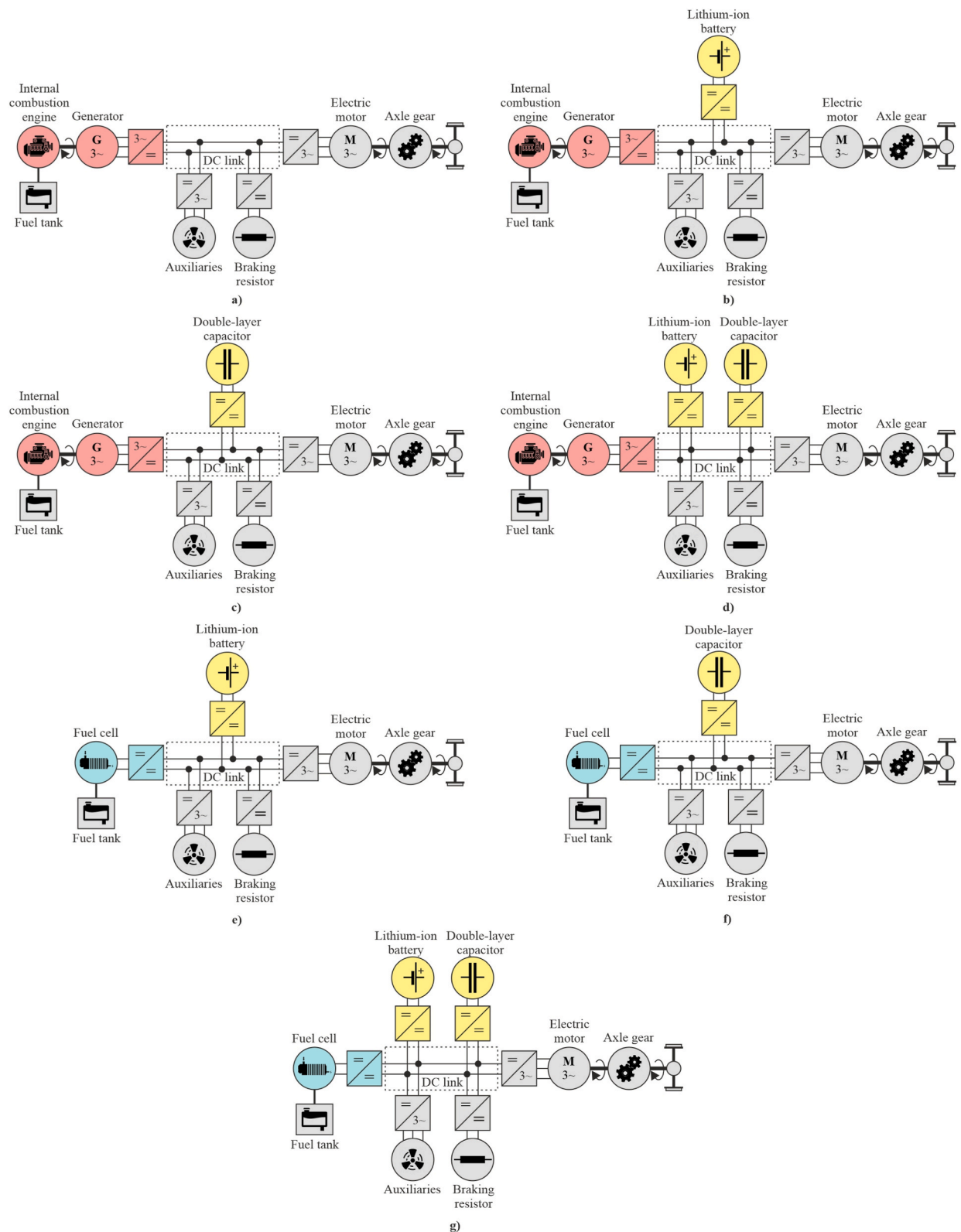
Fig. 1. Schematic representation of alternative propulsion system configurations: (a) standard (non-hybrid); internal combustion engine-based hybrids with (b) lithium-ion battery, (c) double-layer capacitor, and (d) hybrid energy storage system; fuel cell-based hybrids with (e) lithium-ion battery, (f) double-layer capacitor, and (g) hybrid energy storage system.

comparative design and reliable performance assessment is addressing the issues related to detailed data availability and high models complexity.

Considering the previously discussed main aspects, identified knowledge gaps, and the context of the present analysis, the following are defined as the contributions of this paper:

(i) A method to support the design of alternative hydrogen-powered propulsion systems for a regional railway vehicle, including both internal combustion engine and fuel cell system as the prime mover, and various energy storage systems based on lithium-ion battery and/or double-layer capacitor technologies.

(ii) A backward-looking quasi-static simulation model equipped with an achievable real-time energy management and control strategy applicable to all considered powertrain configurations. It allows for realistic systems performance evaluation, while requiring only main technology parameters typically published by manufacturers and avoiding issues related to the detailed data unavailability and/or confidentiality;

(iii) A feasibility study and comparative analysis of fuel economy and greenhouse gas emissions of alternative systems, applied in a case of a two-coach diesel-electric multiple unit employed on a regional railway network in the Netherlands. The results will provide the railway undertaking and decision-makers with an essential input for future investments planning.

3. Hydrogen-powered propulsion systems modelling and control

This section presents the approach used in modelling and control of hydrogen-based propulsion systems, which served as a basis for the overall design analysis. First, alternative propulsion system configurations for a conventional diesel-electric vehicle are introduced, followed by a detailed description of the simulation model that includes the dynamics of individual main system components, and a control strategy used in distributing the power flows between different power sources in the system.

3.1. Propulsion system configurations

The propulsion system of a standard DEMU (Fig. 1a) is based on a series topology consisting of an internal combustion engine (ICE) and two electric machines (Spiryagin et al., 2014). ICE directly connected to an AC electric generator forms an engine-generator unit (EGU), which is further connected via the rectifier and inverter to an AC electric motor located on the driveshaft. The axle gear transmits the power from the electric motor shaft to the wheels with a constant gear ratio. Electric motor enables electro-dynamic braking and its operation as a generator, allowing for recuperation of braking energy. In standard DEMU vehicles, this energy is completely dissipated at the braking resistor (rheostat), connected to the DC link via a DC/DC converter. We assume total electrification of auxiliary systems connected to the existing DC link via a DC/AC inverter. Compared to other systems such as diesel-mechanical or diesel-hydraulic, the electric transmission system, in this case, allows for fully independent rotational speed of the
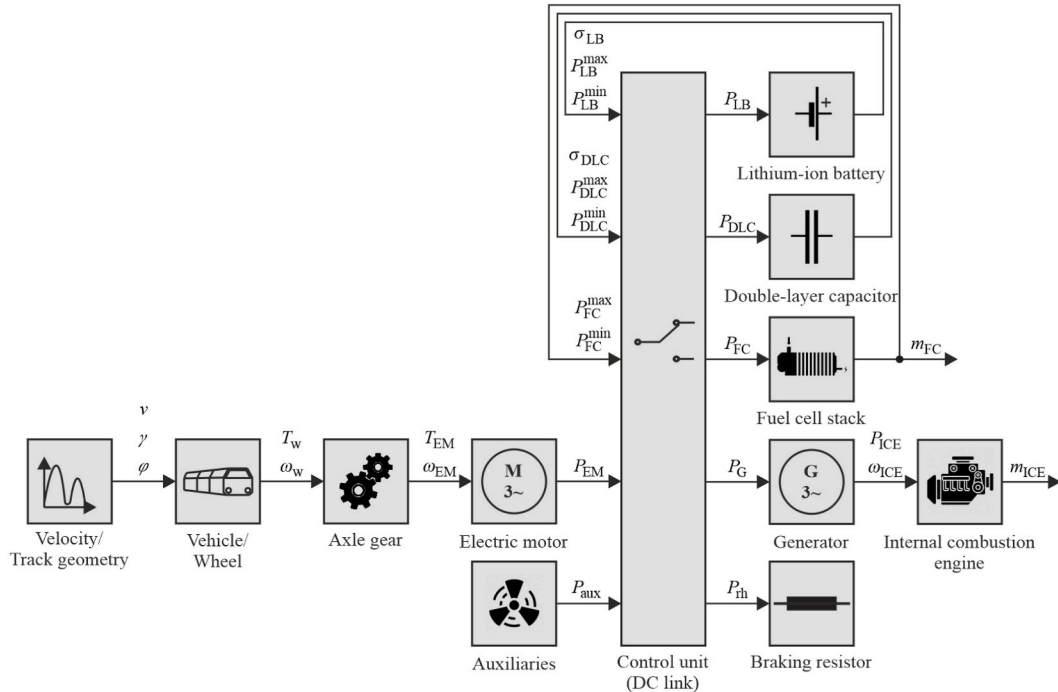

Fig. 2. Structure of the backward-looking simulation model for the alternative hydrogen-based propulsion systems.

ICE from the wheel and its operation in optimal region for a particular power demand level.

Conversion of standard DEMU to its hydrogen-powered counterpart can be achieved by replacing the prime mover of the system architecture, i.e., diesel ICE with hydrogen ICE (Fig. 1a–d), or the EGU and corresponding rectifier with FC stack and unidirectional DC/DC converter (Fig. 1e–g), together with hybridization by adding appropriately sized ESS that would enable recuperation of braking energy and its later use in powering traction and auxiliary systems. Considering non-steady duty cycles of regional passenger trains, rapid development, commercial availability and foreseen decrease in the price of PEMFCs, we limit the analysis in this paper to this particular technology. Three different ESS configurations are considered in this study – LB (Fig. 1b,e), DLC (Fig. 1c,f), and HESS that combine both LB and DLC technologies (Fig. 1d,g). Active control of each ESS technology is achieved via a corresponding bidirectional DC/DC converter. Due to the slow dynamic response of FCs, a non-hybrid configuration powered solely by FCs is not considered, as it would require a significant increase of the FC system size according to the peak power demand and high dissipation of hydrogen energy. This results in seven powertrain configurations shown in Fig. 1a–g.

Compared to diesel fuel, hydrogen is featured with high flammability, and high complexity requirements to store, transport and handle (Dincer and Zamfirescu, 2016). In addition to the previous adjustments in the powertrain structure, converting diesel vehicles to hydrogen-powered counterparts requires replacing conventional fuel tank systems used for standard liquid fuels with an adequate onboard hydrogen storage system. Several technologies are available for onboard hydrogen storage, including high-pressure cylinders (typically 350 or 700 bar), metal hydride storage systems, or systems for liquefied hydrogen through cryo-compression at low temperatures (Madovi et al., 2021).

3.2. Simulation model

The dynamics of alternative system architectures are modeled using a backward-looking quasi-static simulation approach (Kapetanović et al., 2021a; Leska et al., 2017; Pröhl, 2017a). The simulation model is developed with the MATLAB/Simulink tool and OPEUS Simulink toolbox (Pröhl, 2017b). We extend the Simulink toolbox and the model presented by Kapetanović et al. (2021b) with the FC module and corresponding EMCSs for each alternative system. The simulation model structure (Fig. 2) reflects the physical system architectures from Fig. 1, with the individual blocks representing components of the model for the hybrid system. Simulation of different configurations is achieved by disconnecting components not included in the respective system. Corresponding to the backward simulation approach, the inputs of the simulation model are the vehicle velocity and track geometry profiles. The energy-optimized velocity profile is pre-calculated using the bi-section algorithm (Leska et al., 2013), that considers optimal switching points between the acceleration, cruising, coasting and braking phases, while complying with the scheduled running times, track speed limitations, vehicle weight and maximum tractive/braking effort characteristics. A constant passenger load is assumed in determining the vehicle weight. The main output is given by a cumulative fuel consumption during the trip. The arrows indicate the numerical evaluation order of the model components, opposed to the direction of the physical power flow. The power converters in regional railway vehicles are featured with high efficiency, typically above 98% (Giro Batalla and Feenstra, 2012) compared to the main components such as traction motors with efficiencies as low as 70% during low load/low speed operation (Pröhl, 2017b). Thus, following the approach of W. Zhang et al. (2017), only energy losses related to the main powertrain components are considered, with efficiencies of power converters assumed approximately 100%. Nevertheless, converters are considered for the power flows control according to the proposed EMCS (see Section 3.3). A braking resistor is used only for assessing the balance of power flows in the system. The description of the model components is provided in the remainder of this section.

3.2.1. Traction load

Traction load represents the electrical power required by the electric traction motors at the DC link. According to the backward-looking approach, it is fully described by the velocity and track geometry profiles, and the power losses due to inefficiencies of the components along the traction chain, namely of the gearbox and of the electric motor. With the given velocity and track geometry profiles as input signals, longitudinal vehicle dynamics are described by the tractive or braking effort at the wheel $F_w[\text{N}]$, expressed as

$$F_w(v(t)) = m_v \cdot a(t) + R_v(v(t)) + R_g(\gamma(s(t))) + R_c(\varphi(s(t))) \tag{1}$$

with

$$R_v(v(t)) = r_0 + r_1 \cdot v(t) + r_2 \cdot v(t)^2 \tag{2}$$

$$R_g(\gamma(s(t))) = m_v \cdot g \cdot \sin(\gamma(s(t))) \tag{3}$$

$$R_c(\varphi(s(t))) = \begin{cases} m_v \cdot \dfrac{4.91}{\varphi(s(t)) - 30} & \text{if } \varphi(s(t)) \langle 300 \text{ m} \\[3mm] m_v \cdot \dfrac{6.3}{\varphi(s(t)) - 55} & \text{if } \varphi(s(t)) \geq 300 \text{ m,} \end{cases} \tag{4}$$

where $t[\text{s}]$ is the time; $v[\text{m/s}]$ is the vehicle velocity; $s = \displaystyle\int_0^t v(\tau)d\tau[\text{m}]$ is the distance travelled; $a = dv/dt[\text{m/s}^2]$ is the acceleration; $m_v[\text{kg}]$

is the total mass of the vehicle which takes into account the rotary inertia of the powertrain and the passengers weight, i.e. $m_v = (1 + \lambda) \cdot m_{tare} + m_{pax}$, with λ denoting the dimensionless rotating mass factor, $m_{tare}[kg]$ the vehicle tare weight, and $m_{pax}[kg]$ the total weight of passengers; the vehicle resistances $R_v[N]$ include roll resistance and air resistance, modeled as a quadratic function of the vehicle velocity using the Davis equation (Davis, 1926), with vehicle-specific coefficients r_0 [N], $r_1[N/(m/s)]$ and $r_2\left[N/(m/s)^2\right]$; $R_g[N]$ is the grade resistance, with $g = 9.81\left[m/s^2\right]$ representing the gravitational acceleration, and $\gamma[rad]$ the angle of the slope (Brünger and Dahlhaus, 2014); curve resistance $R_c[N]$ is calculated using Roeckl's formula (Huerlimann and Nash, 2003), with $\varphi[m]$ denoting the curve radius. With the given tractive/braking effort at the wheel, traction load is computed according to the numerical evaluation order of the model components shown in Fig. 2, using the following equations (Leska et al., 2017; Pröhl, 2017b):

$$T_w(t) = F_w(v(t)) \cdot \frac{d_w}{2} \tag{5}$$

$$\omega_w(t) = 2 \cdot \frac{v(t)}{d_w} \tag{6}$$

$$T_{EM}(t) = \begin{cases} \dfrac{T_w(t)}{i_{ag} \cdot \eta_{ag}} & \text{if } T_w(t) \geq 0 \\ \dfrac{T_w(t) \cdot \eta_{ag}}{i_{ag}} & \text{if } T_w(t) < 0 \end{cases} \tag{7}$$

$$\omega_{EM}(t) = \omega_w(t) \cdot i_{ag} \tag{8}$$

$$P_{EM}(t) = \begin{cases} \dfrac{T_{EM}(t) \cdot \omega_{EM}(t)}{\eta_{EM}(T_{EM}(t),\ \omega_{EM}(t))} & \text{if } T_{EM}(t) \geq 0 \\ T_{EM}(t) \cdot \omega_{EM}(t) \cdot \eta_{EM}(T_{EM}(t),\ \omega_{EM}(t)) & \text{if } T_{EM}(t) < 0, \end{cases} \tag{9}$$

where $d_w[m]$ denotes the diameter of the powered wheel; $T_w[Nm]$ is the torque at the wheel; $\omega_w[rad/s]$ is the rotational speed of the wheel; i_{ag} is the constant gear ratio; η_{ag} is the efficiency of the gearbox, assumed to be constant; $T_{EM}[Nm]$ is the torque at the mechanical input of the axle gear provided by the electric motor; $\omega_{EM}[rad/s]$ is the rotational speed of the electric motor; $\eta_{EM} = f_{EM}(T_{EM}, \omega_{EM})$ is the efficiency of electric motor, determined by a linear 2D-interpolation in the efficiency map; and $P_{EM}[W]$ is the resulting electric power of the traction motor.

3.2.2. Auxiliary load

In addition to the power required for traction, passenger trains are equipped with auxiliary consumers linked to the propulsion system operation or passengers' comfort. Auxiliary onboard systems include compressors, cooling equipment, heating, ventilation and air conditioning (HVAC), lighting, etc. We model the total auxiliaries power P_{aux} [W] as the sum of the constant term $P_{aux,const}[W]$, representing constant consumers such as lighting and HVAC systems, and the variable term which accounts for the cooling power (Kapetanović et al., 2021b), i.e.

$$P_{aux}(t) = P_{aux,const} + p_{cool} \cdot |P_{EM}(t)|, \tag{10}$$

where coefficient p_{cool} represents the proportion of the total traction power required for cooling the main traction components.

3.2.3. Engine-generator unit

With the given requested electrical power from the EGU, $P_G[W]$, the mechanical output power of the ICE $P_{ICE}[W]$ is computed by

$$P_{ICE} = \frac{P_G}{\eta_G}, \tag{11}$$

with the efficiency $\eta_G = f_G(T_G, \omega_{ICE})$ determined by a linear 2D-interpolation in the efficiency map of the generator. The cumulative
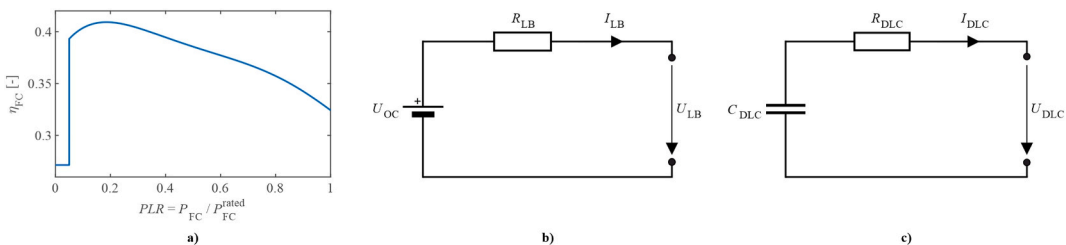

Fig. 3. (a) Efficiency function curve of a fuel cell; equivalent electrical circuits for (b) lithium-ion battery, and (c) double-layer capacitor.

fuel consumption of the ICE, $M_{\mathrm{ICE}}[\mathrm{kg}]$, from the time instant 0 to t, follows from

$$M_{\mathrm{ICE}}(t) = \int_0^t m_{\mathrm{ICE}}(\tau)d\tau = \int_0^t P_{\mathrm{ICE}}(\tau) \cdot \psi(\tau) \cdot d\tau, \tag{12}$$

with the specific fuel consumption $\psi = f(P_{\mathrm{ICE}}, \omega_{\mathrm{ICE}})[\mathrm{kg/Ws}]$ computed using a 2D-linear interpolation of the static engine map (Fig. 5c), based on the instantaneous requested power and the optimal EGU rotational speed $\omega_{\mathrm{ICE}}[\mathrm{rad/s}]$ pre-calculated using the Nelder-Mead simplex method for different possible levels of requested power (Leska et al., 2012).

3.2.4. Fuel cell

A simplified model of a PEMFC is developed to assess hydrogen consumption, while including FC's dynamics and efficiency. With the given requested power from FC, $P_{\mathrm{FC}}(t)$, cumulative hydrogen consumption at time instant t is calculated by (Sarma and Ganguly, 2018):

$$M_{\mathrm{FC}}(t) = \int_0^t m_{\mathrm{FC}}(\tau)d\tau = \int_0^t \frac{P_{\mathrm{FC}}(t)}{LHV_{\mathrm{Hydrogen}} \cdot \eta_{\mathrm{FC}}(PLR(t))} dt, \tag{13}$$

where $\eta_{\mathrm{FC}} = f_{\mathrm{FC}}(PLR(t))$ is the FC efficiency, determined using an approximated function of the normalized FC electrical output power by the rated FC power $P_{\mathrm{FC}}^{\mathrm{rated}}[\mathrm{W}]$, referred to as part-load ratio (PLR), i.e., $PLR = P_{\mathrm{FC}}/P_{\mathrm{FC}}^{\mathrm{rated}}$ (Maleki and Rosen, 2017):

$$\eta_{\mathrm{FC}}(PLR(t)) = \begin{cases} 0.2716 & \text{if } (PLR)\langle 0.05 \\ \begin{aligned} & 0.9033 \cdot (PLR(t))^5 - 2.996 \cdot (PLR(t))^4 \\ & +3.6503 \cdot (PLR(t))^3 - 2.0704 \cdot (PLR(t))^2 \\ & +0.4623 \cdot (PLR(t)) + 0.3747 \end{aligned} & \text{if } (PLR) \geq 0.05. \end{cases} \tag{14}$$

The FC efficiency curve (14) is depicted in Fig. 3a. The slow dynamic response of the PEMFC auxiliary components imposes the limitation on the rate of change of PEMFC output power P_{FC} (Barbir, 2013). Based on the premise that the PEMFC requires 30 s from a start-up to reaching 90% of its rated power (Pesaran et al., 2005), the limitation of the rate of change of PEMFC output power is defined by the following constraint

$$\left| \frac{dP_{\mathrm{FC}}}{dt} \right| \leq 0.03 \cdot P_{\mathrm{FC}}^{\mathrm{rated}} \left[\frac{\mathrm{W}}{\mathrm{s}} \right]. \tag{15}$$

Thus, the maximum and the minimum possible FC power at time instant t, $P_{\mathrm{FC}}^{\max}(t)$ and $P_{\mathrm{FC}}^{\min}(t)$, result from the power load of the FC in the previous time instant, $P_{\mathrm{FC}}(t - \Delta t)$, and the constraint (15).

3.2.5. Lithium-ion battery

A lithium-ion battery (LB) model is implemented for the equivalent electrical circuit shown in Fig. 3b. It consists of an open circuit voltage source $U_{\mathrm{OC}}[\mathrm{V}]$, which depends on the battery state-of-charge (SoC), in series with a constant internal resistance $R_{\mathrm{LB}}[\Omega]$, which represents ohmic losses and depends on the direction of the ESS current $I_{\mathrm{LB}}[\mathrm{A}]$ (i.e., whether the battery is being charged or discharged). With the given power provided from the battery $P_{\mathrm{LB}}[\mathrm{W}]$, the battery current and terminal voltage $U_{\mathrm{LB}}[\mathrm{V}]$ are determined by (Prohl and Aschemann, 2019):

$$I_{\mathrm{LB}}(t) = \frac{U_{\mathrm{OC}}(\sigma_{\mathrm{LB}}(t)) - \sqrt{U_{\mathrm{OC}}(\sigma_{\mathrm{LB}}(t))^2 - 4 \cdot P_{\mathrm{LB}}(t) \cdot R_{\mathrm{LB}}(I_{\mathrm{LB}}(t))}}{2 \cdot R_{\mathrm{LB}}(I_{\mathrm{LB}}(t))} \tag{16}$$

$$U_{\mathrm{LB}}(t) = U_{\mathrm{OC}}(\sigma_{\mathrm{LB}}(t)) - R_{\mathrm{LB}}(I_{\mathrm{LB}}(t)) \cdot I_{\mathrm{LB}}(t). \tag{17}$$

With the initial SoC $\sigma_{\mathrm{LB}}(0)$, and nominal battery capacity $Q_{\mathrm{LB}}[\mathrm{As}]$, the battery SoC at time instant t results from

$$\sigma_{\mathrm{LB}}(t) = \sigma_{\mathrm{LB}}(0) - \frac{1}{Q_{\mathrm{LB}}} \cdot \int_0^t I_{\mathrm{LB}}(\tau)d\tau. \tag{18}$$

The maximum (discharging) power $P_{\mathrm{LB}}^{\max}[\mathrm{W}]$ and minimum (charging) power $P_{\mathrm{LB}}^{\min}[\mathrm{W}]$ are limited by the maximum and minimum current, $I_{\mathrm{LB}}^{\max}[\mathrm{A}]$ and $I_{\mathrm{LB}}^{\min}[\mathrm{A}]$, while keeping the limits of the SoC $\sigma_{\mathrm{LB}} \in [\sigma_{\mathrm{LB}}^{\min}, \sigma_{\mathrm{LB}}^{\max}]$, battery voltage $U_{\mathrm{LB}} \in [U_{\mathrm{LB}}^{\min}, U_{\mathrm{LB}}^{\max}]$, and allowed short peak values (Kapetanović et al., 2021b):

$$P_{\mathrm{LB}}^{\max}(t) = \left(U_{\mathrm{OC}}(\sigma_{\mathrm{LB}}(t)) - R_{\mathrm{LB}}^{\mathrm{dch}} \cdot I_{\mathrm{LB}}^{\max}(t) \right) \cdot I_{\mathrm{LB}}^{\max}(t) \tag{19}$$

$$P_{\mathrm{LB}}^{\min}(t) = \left(U_{\mathrm{OC}}(\sigma_{\mathrm{LB}}(t)) - R_{\mathrm{LB}}^{\mathrm{ch}} \cdot I_{\mathrm{LB}}^{\min}(t) \right) \cdot I_{\mathrm{LB}}^{\min}(t) \tag{20}$$

with

$$I_{\text{LB}}^{\max}(t) = \min\left\{ \frac{U_{\text{OC}}(\sigma_{\text{LB}}(t)) - U_{\text{LB}}^{\min}}{R_{\text{LB}}^{\text{dch}}}, \ \frac{(\sigma_{\text{LB}}(t) - \sigma_{\text{LB}}^{\min}) \cdot Q_{\text{LB}}}{\Delta t}, \ I_{\text{LB}}^{\max,\text{dch}}(t) \right\} \tag{21}$$

$$I_{\text{LB}}^{\min}(t) = \max\left\{ \frac{U_{\text{OC}}(\sigma_{\text{LB}}(t)) - U_{\text{LB}}^{\max}}{R_{\text{LB}}^{\text{ch}}}, \ \frac{(\sigma_{\text{LB}}(t) - \sigma_{\text{LB}}^{\max}) \cdot Q_{\text{LB}}}{\Delta t}, \ I_{\text{LB}}^{\max,\text{ch}}(t) \right\}, \tag{22}$$

where Δt[s] is the simulation (integration) time step, and $I_{\text{LB}}^{\max,\text{dch}}$[A] and $I_{\text{LB}}^{\max,\text{ch}}$[A] are the maximum discharging and charging current, defined by the maximum permitted continuous values ($I_{\text{LB}}^{\text{cont,dch}}$[A],$I_{\text{LB}}^{\text{cont,ch}}$[A]) or the pulse values $\left(I_{\text{LB}}^{\text{peak,dch}}$[A], $I_{\text{LB}}^{\text{peak,ch}}$[A] \right)$ allowed for the limited time ($t_{\text{peak}}^{\text{dch}}$[s], $t_{\text{peak}}^{\text{ch}}$[s]) and controlled by the corresponding time counters ($t_{\text{cnt}}^{\text{dch}}$, $t_{\text{cnt}}^{\text{ch}}$), i.e.

$$I_{\text{LB}}^{\max,\text{dch}}(t) = \begin{cases} I_{\text{LB}}^{\text{peak,dch}} & \text{if } t_{\text{cnt}}^{\text{dch}}(t) < t_{\text{peak}}^{\text{dch}} \\ I_{\text{LB}}^{\text{cont,dch}} & \text{if } t_{\text{cnt}}^{\text{dch}}(t) \geq t_{\text{peak}}^{\text{dch}} \end{cases} \tag{23}$$

$$I_{\text{LB}}^{\max,\text{ch}}(t) = \begin{cases} I_{\text{LB}}^{\text{peak,ch}} & \text{if } t_{\text{cnt}}^{\text{ch}}(t) < t_{\text{peak}}^{\text{ch}} \\ I_{\text{LB}}^{\text{cont,ch}} & \text{if } t_{\text{cnt}}^{\text{ch}}(t) \geq t_{\text{peak}}^{\text{ch}}. \end{cases} \tag{24}$$

3.2.6. Double-layer capacitor

A double-layer capacitor (DLC) model is based on the equivalent circuit shown in Fig. 3c. The circuit is comprised of an internal resistance R_{DLC} [Ω] in series with a capacitance C_{DLC} [F]. Due to the linear relationship between the voltage and SoC of DLC (Li et al., 2019), terminal voltage and current at time instant t can be determined by

$$U_{\text{DLC}}(\sigma_{\text{DLC}}(t)) = \sigma_{\text{DLC}}(t) \cdot (U_{\text{DLC}}^{\max} - U_{\text{DLC}}^{\min}) + U_{\text{DLC}}^{\min}, \tag{25}$$

$$I_{\text{DLC}}(t) = \frac{U_{\text{DLC}}(\sigma_{\text{DLC}}(t)) - \sqrt{U_{\text{DLC}}(\sigma_{\text{DLC}}(t))^2 - 4 \cdot P_{\text{DLC}}(t) \cdot R_{\text{DLC}}}}{2 \cdot R_{\text{DLC}}} \tag{26}$$

where $U_{\text{DLC}}^{\min}$ [V] and $U_{\text{DLC}}^{\max}$ [V] are the minimum and maximum voltage of DLC, respectively. With the initial SoC $\sigma_{\text{DLC}}(0)$, and using (25) and (26) the resulting SoC follows from

$$\sigma_{\text{DLC}}(t) = \sigma_{\text{DLC}}(0) - \frac{1}{C_{\text{DLC}} \cdot (U_{\text{DLC}}^{\max} - U_{\text{DLC}}^{\min})} \cdot \int_0^t I_{\text{DLC}}(\tau)d\tau. \tag{27}$$

The maximum (discharging) and minimum (charging) power of the DLC is limited by the current of the DLC. Either the maximum current is reached in order to keep the voltage constrains $U_{\text{DLC}} \in [U_{\text{DLC}}^{\min}, U_{\text{DLC}}^{\max}]$, or the maximum charging/discharging permitted current defined by the manufacturer ($I_{\text{DLC}}^{\max,\text{dch}}$[A], $I_{\text{DLC}}^{\max,\text{ch}}$[A]) is reached (Kapetanović et al., 2021b):

$$P_{\text{DLC}}^{\max}(t) = U_{\text{DLC}}(\sigma_{\text{DLC}}(t)) \cdot I_{\text{DLC}}^{\max}(t) \tag{28}$$

$$P_{\text{DLC}}^{\min}(t) = U_{\text{DLC}}(\sigma_{\text{DLC}}(t)) \cdot I_{\text{DLC}}^{\min}(t) \tag{29}$$
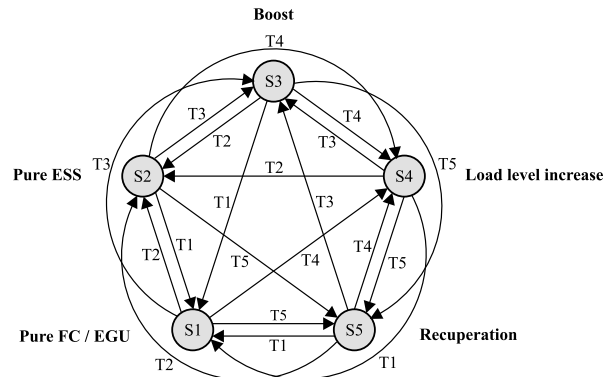

Fig. 4. Power control based on a finite state machine, with indicated five states and corresponding transition triggers.

with

$$I_{\text{DLC}}^{\max}(t) = \min\left\{\frac{\left(U_{\text{DLC}}(\sigma_{\text{DLC}}(t)) - U_{\text{DLC}}^{\min}\right) \cdot C_{\text{DLC}}}{\Delta t}, \ I_{\text{DLC}}^{\max,\text{dch}}\right\} \tag{30}$$

$$I_{\text{DLC}}^{\min}(t) = \max\left\{\frac{\left(U_{\text{DLC}}(\sigma_{\text{DLC}}(t)) - U_{\text{DLC}}^{\max}\right) \cdot C_{\text{DLC}}}{\Delta t}, \ I_{\text{DLC}}^{\max,\text{ch}}\right\}. \tag{31}$$

3.3. Energy management and control strategy

The aim of the EMCS implemented in the control unit (see Fig. 2) is to distribute total instantaneous demanded power for traction and auxiliaries $P_{\text{dem}}(t) = P_{\text{EM}}(t) + P_{\text{aux}}(t)$ between different power sources in the system, while complying with the following main requirements:

(i) Improving fuel economy by maximizing regenerative braking energy and its later use in powering traction and auxiliary systems;
(ii) Increasing overall efficiency of the prime mover (ICE or FC) by avoiding low load operation;
(iii) Supporting the prime mover by an ESS during high power demand phases (acceleration);
(iv) Prolonging the LB life by giving priority to the DLC during charge/discharge processes for the HESS configurations.

To fulfil previous requirements, a real-time control based on a finite state machine (FSM) is proposed, allowing for realistic and achievable estimations of potential fuel savings for different configurations. FSM controls can be easily programmed in micro-controllers (Li et al., 2016), used for dispatching different power sources in the system by controlling their unidirectional or bidirectional converters, thus providing effective and implementable management of complex systems such as hybrid railway vehicles (Han et al., 2017; Yan et al., 2019). A five-state control is proposed (Fig. 4), with states S1–S5 representing typical operation modes of a hybrid system (Kapetanović et al., 2021b), and with the corresponding triggers (conditions) T1–T5 covering all theoretically possible transitions between states, irrespective of the degree of hybridization, i.e., relative rated power ratio between the prime mover and the ESS. To define the operation modes for different states, an optimal level of electrical power from each prime mover is introduced, corresponding to its optimal efficiency region. These reference values are denoted by $P_G^{\text{opt}}[\text{W}]$ and $P_{\text{FC}}^{\text{opt}}[\text{W}]$, for EGU and FC, respectively. Excessive ESS charge from the prime mover and the dissipation of braking energy is avoided by introducing additional SoC reference values for each $\text{ESS} \in (\text{LB}, \text{DLC})$, denoted as $\sigma_{\text{ESS}}^{\lim} \in \left(\sigma_{\text{ESS}}^{\min}, \sigma_{\text{ESS}}^{\max}\right)$. To avoid frequent switches between ESS charging and discharging operation modes that might cause its damage and degradation, a hysteresis cycle for the SoC, $\sigma_{\text{ESS}}^{\text{hyst}} \in \left(\sigma_{\text{ESS}}^{\min}, \sigma_{\text{ESS}}^{\lim}\right)$, is implemented by introducing a dynamic binary indicator $\text{Flag}(t) \in \{0, 1\}$, with $\text{Flag}(0) = 0$.

For the sake of brevity, the power distribution and the triggers for transitions between different states are further presented only for the FCMU with HESS, as the most complex case. Analogously, the power distribution strategy for the remaining hybrid configurations represents a simplified case of the control (32)–(41). Single-technology ESS configurations are controlled by excluding parameters and terms related to the ESS technology not included in the observed system. For ICE-based configurations, all terms related to the FC system are replaced with the EGU-related equivalent, i.e., $P_G(t), P_G^{\text{opt}}, P_G^{\text{idle}} = 0, P_G^{\min} = 0, P_G^{\max} = const$.

Under the *Pure FC state* (S1), total demanded power $P_{\text{dem}}(t)$ is provided by FC system, and the ESS converters are switched off. Depending on the requested power level, FC output power limits, and ESS SoC and maximum power, this state is active under conditions defined by

$$T1: \begin{aligned} &P_{\text{FC}}^{\min}(t) \leq P_{\text{dem}}(t) \leq P_{\text{FC}}^{\max}(t) \\ &\wedge (P_{\text{dem}}(t) = P_{\text{FC}}^{\text{opt}} \vee \left(P_{\text{dem}}(t) > P_{\text{FC}}^{\text{opt}} \wedge \sigma_{\text{DLC}}(t) = \sigma_{\text{DLC}}^{\min} \wedge \sigma_{\text{LB}}(t) = \sigma_{\text{LB}}^{\min}\right) \\ &\vee \left(P_{\text{dem}}(t) < P_{\text{FC}}^{\text{opt}} \wedge P_{\text{dem}}(t) > \left(P_{\text{DLC}}^{\max}(t) + P_{\text{LB}}^{\max}(t)\right) \wedge \sigma_{\text{DLC}}(t) \geq \sigma_{\text{DLC}}^{\lim} \wedge \sigma_{\text{LB}}(t) \geq \sigma_{\text{LB}}^{\lim}\right)) \end{aligned} \tag{32}$$
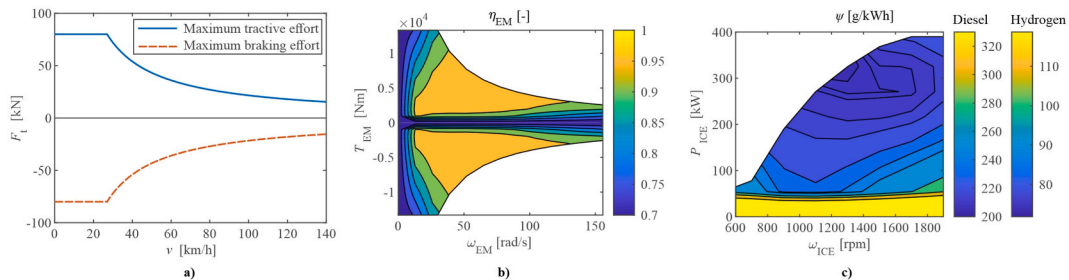

Fig. 5. (a) Maximum tractive and braking effort; (b) reconstructed efficiency map of an electric motor; and (c) specific fuel consumption map of an internal combustion engine for the Stadler GTW 2/6 multiple-unit vehicle.

$$S1 : \begin{cases} P_{\text{FC}}(t) = P_{\text{dem}}(t) \\ P_{\text{DLC}}(t) = 0 \\ \qquad P_{\text{LB}}(t) = 0 \\ Flag(t) = Flag(t - \Delta t). \end{cases} \tag{33}$$

In the *Pure ESS state* (S2), the ESS provides the total requested power, with FC switched to idle. The corresponding conditions and power flows are defined by

$$T2 : \; \left(0 \leq P_{\text{dem}}(t) \leq \left(P_{\text{DLC}}^{\max}(t) + P_{\text{LB}}^{\max}(t)\right)\right) \wedge \left(Flag(t - \Delta t) = 0 \vee \left(Flag(t - \Delta t) = 1 \wedge \left(\sigma_{\text{DLC}}(t) \geq \sigma_{\text{DLC}}^{\text{hyst}} \wedge \sigma_{\text{LB}}(t) \geq \sigma_{\text{LB}}^{\text{hyst}}\right)\right)\right) \tag{34}$$

$$S2 : \begin{cases} P_{\text{FC}}(t) = \max\left\{P_{\text{FC}}^{\min}(t), P_{\text{FC}}^{\text{idle}}\right\} \\ P_{\text{DLC}}(t) = \min\left\{P_{\text{DLC}}^{\max}(t), P_{\text{dem}}(t)\right\} \\ P_{\text{LB}}(t) = P_{\text{dem}}(t) - P_{\text{DLC}}(t) \\ \qquad Flag(t) = 0. \end{cases} \tag{35}$$

In the *Boost state* (S3), ESS provides support for the FC by providing a portion of high requested power that exceeds its maximum disposable power, i.e.

$$T3 : \begin{aligned} &\left(\left(P_{\text{dem}}(t) < P_{\text{FC}}^{\text{opt}} \wedge P_{\text{dem}}(t) > P_{\text{FC}}^{\max}(t)\right) \vee P_{\text{dem}}(t) > P_{\text{FC}}^{\text{opt}}\right) \\ &\wedge P_{\text{dem}}(t) > \left(P_{\text{DLC}}^{\max}(t) + P_{\text{LB}}^{\max}(t)\right) \wedge \left(\sigma_{\text{DLC}}(t) > \sigma_{\text{DLC}}^{\min} \vee \sigma_{\text{LB}}(t) > \sigma_{\text{LB}}^{\min}\right) \\ &\wedge \left(Flag(t - \Delta t) = 0 \vee \left(Flag(t - \Delta t) = 1 \wedge \sigma_{\text{DLC}}(t) \geq \sigma_{\text{DLC}}^{\text{hyst}} \wedge \sigma_{\text{LB}}(t) \geq \sigma_{\text{LB}}^{\text{hyst}}\right)\right) \end{aligned} \tag{36}$$

$$S3 : \begin{cases} P_{FC}(t) = \min\left\{\max\left\{\left(P_{\text{dem}}(t) - P_{\text{DLC}}^{\max}(t) - P_{\text{LB}}^{\max}(t)\right), P_{\text{FC}}^{\min}(t), P_{\text{FC}}^{\text{opt}}\right\}, P_{\text{FC}}^{\max}(t)\right\} \\ P_{\text{DLC}}(t) = \min\left\{\left(P_{\text{dem}}(t) - P_{\text{FC}}(t)\right), P_{\text{DLC}}^{\max}(t)\right\} \\ P_{\text{LB}}(t) = P_{\text{dem}}(t) - P_{\text{FC}}(t) - P_{\text{DLC}}(t) \\ \qquad Flag(t) = 0. \end{cases} \tag{37}$$

Under the *Load level increase state* (S4), featured with low power demand, the FC provides the excess power which is used for recharging the ESS, defined by

$$T4 : \begin{aligned} &\left(P_{\text{dem}}(t) < P_{\text{FC}}^{\text{opt}} \wedge P_{\text{dem}}(t) \leq P_{\text{FC}}^{\max}(t) \wedge P_{\text{dem}}(t) > \left(P_{\text{DLC}}^{\max}(t) + P_{\text{LB}}^{\max}(t)\right) \wedge \left(\sigma_{\text{DLC}}(t) < \sigma_{\text{DLC}}^{\text{lim}} \vee \sigma_{\text{LB}}(t) < \sigma_{\text{LB}}^{\text{lim}}\right)\right) \\ &\vee \left(0 \leq P_{\text{dem}}(t) < P_{\text{FC}}^{\text{opt}} \wedge P_{\text{dem}}(t) \leq P_{\text{FC}}^{\max}(t) \wedge P_{\text{dem}}(t) \leq \left(P_{\text{DLC}}^{\max}(t) + P_{\text{LB}}^{\max}(t)\right)\right) \\ &\wedge Flag(t - \Delta t) = 1 \wedge \left(\sigma_{\text{DLC}}(t) < \sigma_{\text{DLC}}^{\text{hyst}} \vee \sigma_{\text{LB}}(t) < \sigma_{\text{LB}}^{\text{hyst}}\right)) \end{aligned} \tag{38}$$

$$S_4 \begin{cases} P_{\text{FC}}(t) = \min\left\{\max\left\{P_{\text{FC}}^{\min}(t), P_{\text{FC}}^{\text{opt}}\right\}, P_{\text{FC}}^{\max}\right\} \\[6pt] P_{\text{DLC}}(t) = \begin{cases} \max\left\{\left(P_{\text{dem}}(t) - P_{\text{FC}}(t)\right), P_{\text{DLC}}^{\min}(t)\right\} & \text{if } \left(P_{\text{dem}}(t) > \left(P_{\text{DLC}}^{\max}(t) + P_{\text{LB}}^{\max}(t)\right) \wedge \sigma_{\text{DLC}}(t) < \sigma_{\text{DLC}}^{\text{lim}}\right) \\ \qquad \vee \left(P_{\text{dem}}(t) \leq \left(P_{\text{DLC}}^{\max}(t) + P_{\text{LB}}^{\max}(t)\right) \wedge Flag(t - \Delta t) = 1 \wedge \sigma_{\text{DLC}}(t) < \sigma_{\text{DLC}}^{\text{hyst}}\right) \\ 0 \quad \text{if } \left(P_{\text{dem}}(t) > \left(P_{\text{DLC}}^{\max}(t) + P_{\text{LB}}^{\max}(t)\right) \wedge \sigma_{\text{DLC}}(t) \geq \sigma_{\text{DLC}}^{\text{lim}}\right) \\ \qquad \vee \left(P_{\text{dem}}(t) \leq \left(P_{\text{DLC}}^{\max}(t) + P_{\text{LB}}^{\max}(t)\right) \wedge Flag(t - \Delta t) = 1 \wedge \sigma_{\text{DLC}}(t) \geq \sigma_{\text{DLC}}^{\text{hyst}}\right) \end{cases} \\[6pt] P_{\text{LB}}(t) = \begin{cases} \max\left\{\left(P_{\text{dem}}(t) - P_{\text{FC}}(t) - P_{\text{DLC}}(t)\right), P_{LB}^{\min}(t)\right\} & \text{if } \left(P_{\text{dem}}(t) > \left(P_{\text{DLC}}^{\max}(t) + P_{\text{LB}}^{\max}(t)\right) \wedge \sigma_{\text{LB}}(t) < \sigma_{\text{LB}}^{\text{lim}}\right) \\ \qquad \vee \left(P_{\text{dem}}(t) \leq \left(P_{\text{DLC}}^{\max}(t) + P_{\text{LB}}^{\max}(t)\right) \wedge Flag(t - \Delta t) = 1 \wedge \sigma_{\text{LB}}(t) < \sigma_{\text{LB}}^{\text{hyst}}\right) \\ 0 \quad \text{if } \left(P_{\text{dem}}(t) > \left(P_{\text{DLC}}^{\max}(t) + P_{\text{LB}}^{\max}(t)\right) \wedge \sigma_{\text{LB}}(t) \geq \sigma_{\text{LB}}^{\text{lim}}\right) \\ \qquad \vee \left(P_{\text{dem}}(t) \leq \left(P_{\text{DLC}}^{\max}(t) + P_{\text{LB}}^{\max}(t)\right) \wedge Flag(t - \Delta t) = 1 \wedge \sigma_{\text{LB}}(t) \geq \sigma_{\text{LB}}^{\text{hyst}}\right) \end{cases} \\[6pt] Flag(t) = 1. \end{cases} \tag{39}$$

The *Recuperation state* (S5) is active during braking, with the negative power values at the DC link used for recharging the ESS. The power distributed to the ESS is limited with its maximum charging power, with the excess power dissipated at the braking rheostat, and FC switched to idle and corresponding DC/DC converter switched off, i.e.

$$T5 : P_{\text{dem}}(t) < 0 \tag{40}$$

$$S5 : \begin{cases} P_{\text{DLC}}(t) = \max\left\{P_{\text{DLC}}^{\min}(t), P_{\text{dem}}(t)\right\} \\ P_{\text{LB}}(t) = \max\left\{P_{\text{LB}}^{\min}(t), (P_{\text{dem}}(t) - P_{\text{DLC}}(t))\right\} \\ P_{\text{FC}}(t) = \max\left\{P_{\text{FC}}^{\min}(t), P_{\text{FC}}^{\text{idle}}\right\} \\ \quad Flag(t) = Flag(t - \Delta t). \end{cases} \tag{41}$$

4. Design and analysis of alternative propulsion systems

This section presents conceptual design and comparative assessment of the seven propulsion system configurations shown in Fig. 1. The systems design comprises sizing of individual components for a benchmark standard DEMU vehicle employed on a selected benchmark route, based on estimated duty cycle coupled with the additional design criteria reflecting main physical and operation constraints. Alternative configurations are then compared in terms of fuel consumption and produced GHG emissions.

4.1. Benchmark vehicle selection

A two-coach version DEMU from the series Gelenktriebwagen (GTW 2/6), currently utilized in the Northern lines (Stadler, 2005), is selected as the benchmark vehicle for this study. GTW is a series of single-decker articulated DEMU regional trains manufactured by Stadler, with hundreds of vehicles in several configurations employed on regional railway lines across Europe and the United States (Stadler, 2021). This is reflected in their high representation in the literature as a reference vehicle on various analyses (Hoffrichter et al., 2016; Kapetanović et al., 2021a, 2021b). Required main input parameters for the selected benchmark vehicle are provided in Table 1. The maximum tractive effort curve, used for pre-calculating the velocity profile as the main simulation input, is shown in Fig. 5a, with negative values assumed for braking. The efficiency map of an electric motor (Fig. 5b) is reconstructed from the normalized efficiency maps provided by Paukert (2011) and Pröhl (2017b). The same sources are used in reconstructing the efficiency map of a generator and the specific consumption map of a diesel ICE (Fig. 5c), where similarly sized ICE is scaled to the one found in GTW 2/6 DEMU using Willan's lines technique (Pourabdollah et al., 2013). With the premise of maintaining the power characteristics (i.e., ICE output power), the specific consumption map of a hydrogen ICE is reconstructed by linearly scaling the specific consumption map of a diesel ICE using the following relation: $\psi_{\text{Hydrogen}}(P_{\text{ICE}}, \omega_{\text{ICE}}) = \psi_{\text{Diesel}}(P_{\text{ICE}}, \omega_{\text{ICE}}) \cdot LHV_{\text{Diesel}} / LHV_{\text{Hydrogen}}$, where $LHV_{\text{Diesel}} = 43.1 [\text{MJ/kg}]$ and $LHV_{\text{Hydrogen}} = 120 [\text{MJ/kg}]$ are the low heating values for diesel and hydrogen, respectively (JRC, 2020a).

Table 1
Characteristics and simulation parameters for the standard GTW 2/6 diesel-electric multiple unit.[a]

Parameter	Unit	Value
Vehicle tare weight[b]	t	70.4
Rotating mass factor[c]	–	0.05
Total passengers weight[d]	t	7
Davis equation coefficient (constant term)[c]	N	1001
Davis equation coefficient (linear term)[c]	N/(km/h)	22.3
Davis equation coefficient (quadratic term)[c]	N/(km/h)^2	0.1
Powered wheel diameter[e]	m	0.86
Axle gear ratio[f]	–	1.7218
Axle gear efficiency[g]	–	0.97
Maximum velocity[e]	km/h	140
Maximum acceleration[c]	m/s^2	1.05
Maximum deceleration[c]	m/s^2	−1
Maximum (starting) tractive effort[e]	kN	80
Maximum power at the wheel[e]	kW	600
Rated power of an electric motor[b]	kW	2 × 400
Rated power of an internal combustion engine[b]	kW	2 × 390
Constant auxiliaries power[d]	kW	50
Cooling power coefficient[d]	–	0.01

Note/Source.
[a] Vehicle parameters also reported by Kapetanović et al. (2021b).
[b] Giro Batalla and Feenstra (2012).
[c] Personal communication with Arriva employees.
[d] Assumed values.
[e] Stadler (2005).
[f] Determined from the ratio between the maximum rotational speed of the GTW's electric motor given by Giro Batalla and Feenstra (2012) and the maximum rotational speed of the wheel corresponding to the maximum vehicle speed.
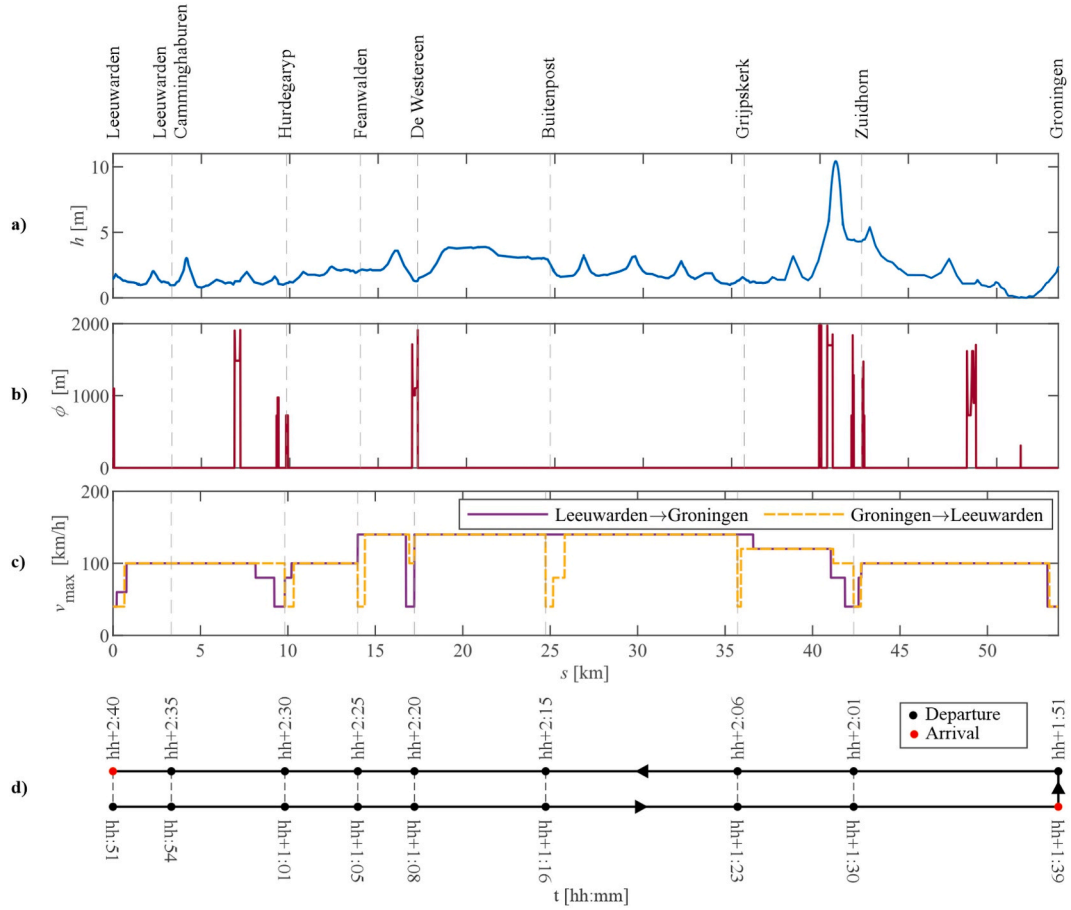[g] Adopted from Pröhl (2017b).

Fig. 6. Railway line Leeuwarden – Groningen: (a) track height compared to Normal Amsterdam Level; (b) position and dimeter of track curves; (c) maximum allowed speed; and (d) train departure times for the two opposite directions.

4.2. Benchmark route selection

The railway line that connects the cities Leeuwarden and Groningen is selected for the train simulations. This 54.051 km long line with seven intermediate stops is the main line in the observed regional network, with the highest utilization level. Due to the difference in line resistances (see Fig. 6a and b) and maximum speed limits for the two opposite directions (Fig. 6c), the vehicle round trip is analyzed, based on the actual periodic timetable and vehicle circulation plan (Fig. 6d). A dwell time of 30 s is assumed at intermediate stops, based on empirical observations, while layover times at the terminal stops are 11 min in Leeuwarden and 12 min in Groningen.
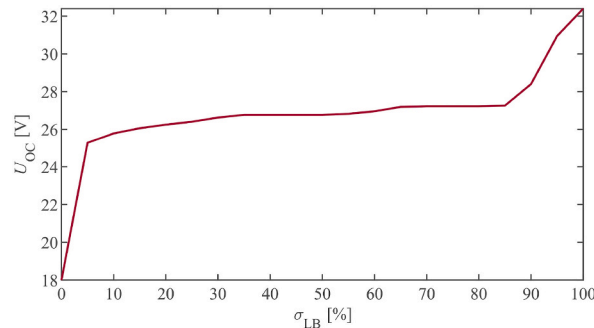
Fig. 7. Reconstructed open circuit voltage function for a lithium-ion battery module.

Table 2
Parameters of different propulsion system components.

Parameter	Unit	Value
Fuel cell module[a]		
Rated power	kW	70
Idle power	kW	8
Volume	m^3	0.61362
Weight	kg	250
Lithium-ion battery module[b,c]		
Nominal capacity	Ah	45
Minimum/maximum continuous current	A	−160/160
Minimum/maximum pulse current	A	−350/350
Allowed time for pulse current	s	10
Minimum/maximum voltage	V	18/32.4
Internal resistance charge/discharge	Ω	0.006/0.006
Minimum/maximum state-of-charge[d]	%	10/90
Energy content	kWh	1.24
Useable energy content[e]	kWh	0.922
Minimum/maximum power at mean state-of-charge[f]	kW	−4.130/4.437
Volume	m^3	0.00857
Weight	kg	15
Double-layer capacitor module[b,g]		
Rated capacitance	F	63
Minimum/maximum continuous current	A	−240/240
Minimum/maximum voltage	V	12.5/125
Internal resistance	Ω	0.018
Energy content	kWh	0.14
Minimum/maximum power at mean state-of-charge[h]	kW	−16.5/16.5
Volume	m^3	0.00546
Weight	kg	61
Hydrogen storage[i]		
Storage capacity	kg	7.8
Volume	m^3	0.418
Tank weight	kg	141

Note/Source.
[a] Extracted/calculated from specifications and data sheets from Ballard (2021).
[b] Also reported by Kapetanović et al. (2021b).
[c] Extracted/calculated values from specifications and data sheets from Toshiba (2021) unless otherwise indicated.
[d] Adopted values for simulation purposes.
[e] Based on allowed SoC range.
[f] Calculated for continuous values using (19)-(22).
[g] Extracted/calculated values from specifications and data sheets from Maxwell (2021) unless otherwise indicated.
[h] Calculated using (28)-(31).
[i] Extracted/calculated from specifications and data sheets from Luxfer (2020b).

4.3. Technology selection

The design approach described in Section 3.1 is conducted using the following assumptions and selected technology. Due to the unavailability of data for a hydrogen ICE, we assume the possibility of converting the existing diesel ICE, or replacing it with hydrogen ICE with identical characteristics in terms of rated power, weight and dimensions. Commercially available technology for LBs, DLCs, FCs and hydrogen storage are considered, thus allowing for realistic estimations. Existing modules are then combined in series/parallel in order to meet the power and energy requirements. FC module FCmove™-HD from Ballard is considered as the replacement technology for EGU. This Ballard's latest platform for heavy-duty power modules based on the FCgen®-LCS stack offers benefits reflected in lower life cycle costs, simplified system integration and high performance (Ballard, 2021). SCiB™ module, type 1–23, of Japanese manufacturer Toshiba, is selected as the LB technology. The module contains 24 Li-ion cells, arranged in 2 parallel branches with 12 cells in series. The cells are based on lithium nickel manganese cobalt oxide (NMC) chemistry with a lithium titanium oxide (LTO) anode, and offer a good compromise between energy density, power density and achievable lifetime (Takami et al., 2013; Toshiba, 2021). Due to the unavailability of the open-circuit voltage characteristic as a function of SoC, data from (SAFT and UNEW, 2017) is adopted and scaled according to voltage limits for the SCiB™ module (Fig. 7). The BMOD0063 module from the manufacturer Maxwell Technologies is selected as DLC technology. It contains 48 cells, with 6 parallel series of 8 cells each. This commercially available module is especially suited for heavy-duty transport applications, such as trains and busses (Maxwell, 2021; Schmid et al., 2017). Luxfer G-Stor™ H2 are the type 3 cylinders for the storage of compressed hydrogen with demonstrated applications in railway vehicles (Luxfer, 2020a). We consider the model W322H35 with 350 bar of pressure since it offers high storage capacity and relatively low weight (Luxfer, 2020b). Detailed characteristics of the selected propulsion system components are given in Table 2.
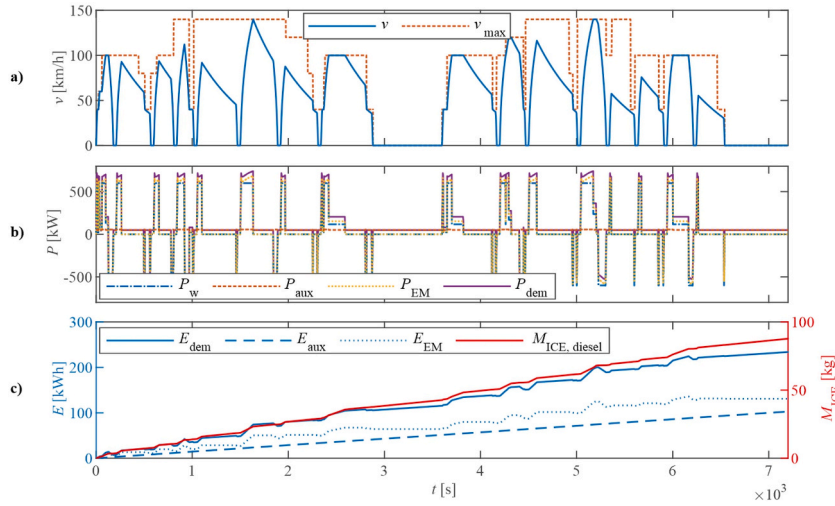
Fig. 8. Simulation results for a benchmark diesel-electric multiple unit: (a) velocity profile; (b) power profiles at the DC link; (d) cumulative energy consumption at the DC link and cumulative consumption of diesel.

Table 3

Summary of round trip duty cycle characteristics (DC link) for the benchmark diesel-electric multiple unit.

Event	Average power [kW]	Peak power [kW]	Duration [s]	Cumulative energy [kWh]
Round trip (Engine-generator unit)	149.1	741.5	7200	298.3
Round trip (DC link)	116.8	741.5	7200	233.7
Acceleration	657.3	741.5	1060	193.1
Gradeability	191.7	363.9	678	36.1
Braking	−456.2	−526.0	510	−64.6
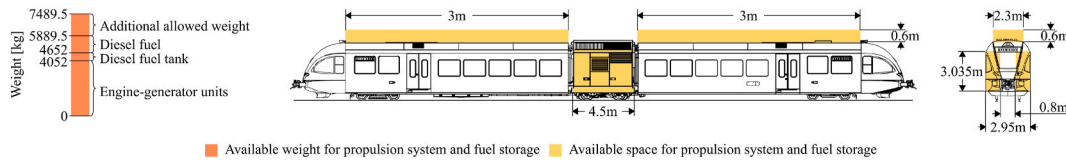
Fig. 9. Graphical representation of a Stadler GTW 2/6 diesel-electric multiple unit with space and weight limitations for propulsion system and hydrofen fuel storage.

4.4. Powertrain components sizing for alternative system configurations

The first step in designing alternative configurations is to define the benchmark criteria in sizing powertrain components. In order to derive power and energy requirements for the new systems, simulation of the round trip for the benchmark DEMU is performed by evaluating the simulation model from Fig. 2, with the total demanded power provided solely by EGU. Fig. 8 shows the speed profile as the main simulation input, power profiles at the wheel and the DC link, and cumulative energy and fuel consumption during the trip, with an estimated total diesel consumption of 87.78 kg. Overall results in terms of average and peak power, and cumulative energy demand, are summarized in Table 3. As can be noted, the braking energy and the difference between the average and peak power values indicate significant potential for hybridization.

To prevent compromising the current timetable, power sources in place, both prime movers and ESSs, should be able to provide the same power and energy required for traction and auxiliaries, and at the same time to allow for the recuperation of the available braking energy. However, the maximum size for the components is conditioned by the maximum allowed weight to satisfy the axle load limitations and the maximum available volumetric space. According to the difference between alternative systems configurations described in Section 3.1, additional weight and volumetric space become available after removing the diesel EGUs and diesel fuel tank. Furthermore, the main criteria influencing fuel storage sizing is maintaining the vehicle range and current timetable, in this case, reflected in operation without refueling during one day, i.e. nine round trips. Fig. 9 shows the graphical representation of a Stadler GTW 2/6 DEMU with indicated space and weight limitations for the propulsion system and hydrogen fuel storage, generated based on the information from Giro Batalla and Feenstra (2012), Hoffrichter et al. (2016), Stadler (2005), and personal communication with Arriva. The derived benchmark criteria are summarized in Table 4.

Table 4

Benchmark criteria in sizing powertrain components.

Parameter	Value	Unit
Energy demand		
Energy at DC link for 9 round trips (without regenerative braking)	2684.7	kWh
Energy at DC link for 9 round trips (with regenerative braking)	2103.3	kWh
Average energy during single acceleration	10.7	kWh
Average energy during single braking	−3.6	kWh
Mass		
Engine-generator units[a]	4052	kg
Diesel fuel tank empty mass[b]	600	kg
Diesel fuel (1500 L)[c]	1237.5	kg
Additional allowed mass (considering total mass limit of 72t)[d]	1600	kg
Total allowed mass	7489.5	kg
Volume		
Engine-generator units[b]	5	m³
Diesel fuel tank	1.5	m³
Additional space available at the roof[d]	8.28	m³
Total available space	14.78	m³

Note/Source.
[a] Giro Batalla and Feenstra (2012).
[b] Approximate values based on personal communication with Arriva employees.
[c] Calculated from the fuel tank capacity provided by Giro Batalla and Feenstra (2012), and diesel fuel density of 0.825 kg/L (Pröhl, 2017b).
[d] Adopted for GTW 2/6 from Hoffrichter et al. (2016).

Due to unavailability of the data related to the safety requirements for different powertrain components, and technical specifications and dimensions of corresponding power converters, safety distances and weight and volumetric space requirements for power electronics devices are not accounted. Since the considered commercial FC, LB and DLC modules already have integrated main auxiliary components (e.g. cooling, monitoring, and cell voltage management), the weight and volumetric space required for auxiliary systems are omitted in the analysis. Nevertheless, we assume that the requirements for both safety distances and any additional auxiliary components can be compensated with the additional available space under the floor (Schmid et al., 2017) and/or by reducing the passenger capacity and utilizing part of the passenger compartments, as applied in the UK's HydroFLEX regional train (Calvert et al., 2021). Furthermore, we assume that required power electronics devices can be integrated into the existing insulated-gate bipolar transistor (IGBT) converter (ABB, 2018) and/or by utilizing the previously discussed additional space. Regarding traction motors, maintaining the two existing traction motors is considered for all powertrain configurations, without changes in their number or characteristics.

Coupling previously defined benchmark criteria with the parameters for different technologies allows for determining the size of each of the components for alternative system configurations. Sizing is realized in the following order: (1) prime mover (EGU or FC), (2) ESS, and (3) hydrogen storage system. Regarding the ICE-based configurations, we assume identical number and characteristics of the EGUs to those found in the standard vehicle. For FC-based configurations, the number of FC modules is defined to satisfy gradeability power, following the recommendation of Garcia et al. (2010). Criteria in dimensioning ESS systems for ICE-based configurations include the peak braking power and average energy for braking. For FC-based alternatives, peak power and average energy values for both braking and acceleration are considered, to account for slow dynamics of an FC system and ensure maintaining tractive characteristics of a vehicle. ESS size is thus determined as the minimum number of modules required to satisfy all of the previously defined criteria. For HESS configurations, LB is sized according to the average power and energy level, while DLC covers the remaining peak power.

Finally, the size of the hydrogen storage system is determined using the following approach. First, the initial number of hydrogen

Table 5

Characteristics of alternative system configurations complying with the maximum range requirement.

Component	Number of components per configuration						
	1	2	3	4	5	6	7
Engine-generator unit	2	2	2	2	–	–	–
Fuel cell module	–	–	–	–	6	6	6
Lithium-ion battery module	–	128	–	111	157	–	149
Double-layer capacitor module	–	–	32	5	–	77	6
Hydrogen fuel cylinder	37	27	29	27	23	25	23
Total mass required [kg]	9557.6	9989.6	10,319.2	10,039.6	7277.4	9917.0	7523.4
Mass constraint met	No	No	No	No	Yes	No	No
Total volume required [m³]	20.47	17.38	17.30	17.26	14.64	14.55	14.61
Volume constraint met	No	No	No	No	Yes	Yes	Yes

cylinders is derived from the energy required at the DC link for nine round trips (Table 4), divided by the efficiency of the prime mover. For the EGU, an efficiency of 28.4% is determined from the ratio of the energy content of the total diesel fuel consumed and cumulative electrical energy provided by the EGU (Table 3), while for the FC the value of 37.8% is adopted as the average efficiency for the operation range between idling and rated FC power (Eq. (14) and Table 2), giving an initial size of 37, 29 and 22 cylinders for standard (non-hybrid), ICE-based hybrid and FC-based hybrid system, respectively. Due to the difference in vehicle weight, and the influence of the EMCS on the final fuel consumption, the final number of cylinders for each propulsion system is determined using an alternating coordination algorithm (Silvas et al., 2016) as follows. Using the initial hydrogen storage system size and the model described in Section 3, hydrogen consumption is evaluated and required number of cylinders for nine round trips is recalculated. In the case of an adjusted number of cylinders, the procedure is repeated until the hydrogen consumption and corresponding required vehicle range have converged.

A summary of obtained alternative system configurations is given in Table 5. As noted, only FCMU with LB satisfies both mass and volume constraints, while the remaining two FC-based configurations exceed only mass limit. Both limits are exceeded for all four ICE-based configurations. Nevertheless, assuming the possibility of increasing axle-load limitation by, e.g., replacing the existing with higher-load axles and/or redistributing the components and vehicle center of gravity, they are further evaluated in terms of potential fuel savings and reduction of GHG emissions. In case the latter solution is not viable, results are further derived for reduced vehicle range scenarios.

4.5. Comparative assessment

4.5.1. Vehicle configurations complying with the maximum range requirement

Previously defined alternative configurations are assessed in terms of hydrogen consumption using the presented model and corresponding parameters for each scenario. Fig. 10 shows the simulation results for the FCMU equipped with a HESS, as the most complex case. Results include vehicle speed profile, power profiles from different components in the system, ESS SoC, and cumulative fuel consumption during the trip. An example of a selected track segment between the two consecutive stops Buitenpost and Grijpskerk shows the system dynamics and power distribution between present sources according to ECMS-defined states. The slow dynamics feature of the FC system is emphasized during the acceleration and braking phases. For the sake of brevity, detailed simulation results for all scenarios are given in Fig. 11, with the estimated hydrogen consumption summarized in Table 6.

As expected, results indicate the highest fuel consumption for non-hybrid configuration with ICE as the prime mover, due to dissipation of braking energy and total demanded power provided solely by EGU. FCMU with LB demonstrated the highest fuel-saving potential, with consumption reduced by 37.9% compared to the standard vehicle. A very similar performance is reached by FCMU equipped with HESS. Although this configuration did not satisfy the mass constraint, the excess of ~34 kg, in this case, can be considered negligible. Despite the limitation of the FC system in terms of slow dynamic response, the overall results indicate significantly better performance of FCMUs compared to the ICE-powered vehicles, mainly due to the higher efficiency of FC systems compared to the EGUs. Regarding hybrid configurations, vehicles equipped with LB demonstrated the highest potential benefits, followed by the HESS, while configuration hybridized solely with the DLC demonstrated higher fuel consumption for both ICE and FC-based vehicles.

4.5.2. Vehicle configurations complying with weight and volumetric space constraints

In case that defined vehicle weight and volumetric space constraints cannot be relaxed, we further adjust the vehicle configurations by reducing the size of the hydrogen storage system, while maintaining the previously defined propulsion system components. The adjusted hydrogen storage system size is determined as the maximum number of cylinders that satisfies both vehicle mass and volumetric space constraints. Since this leads to reduced vehicle range, we assume an efficient refueling system in place, that would prevent compromising the current timetable and vehicle circulation plan.
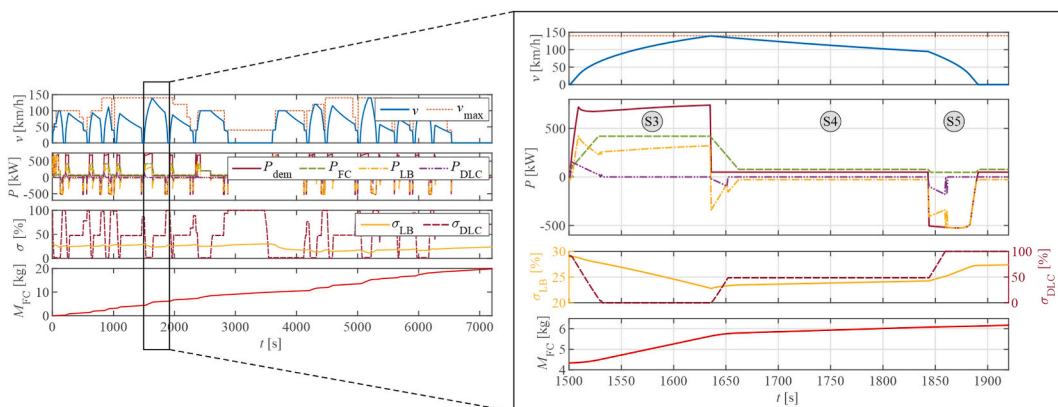

Fig. 10. Simulation results for a fuel cell multiple unit vehicle equipped with a hybrid energy storage system.
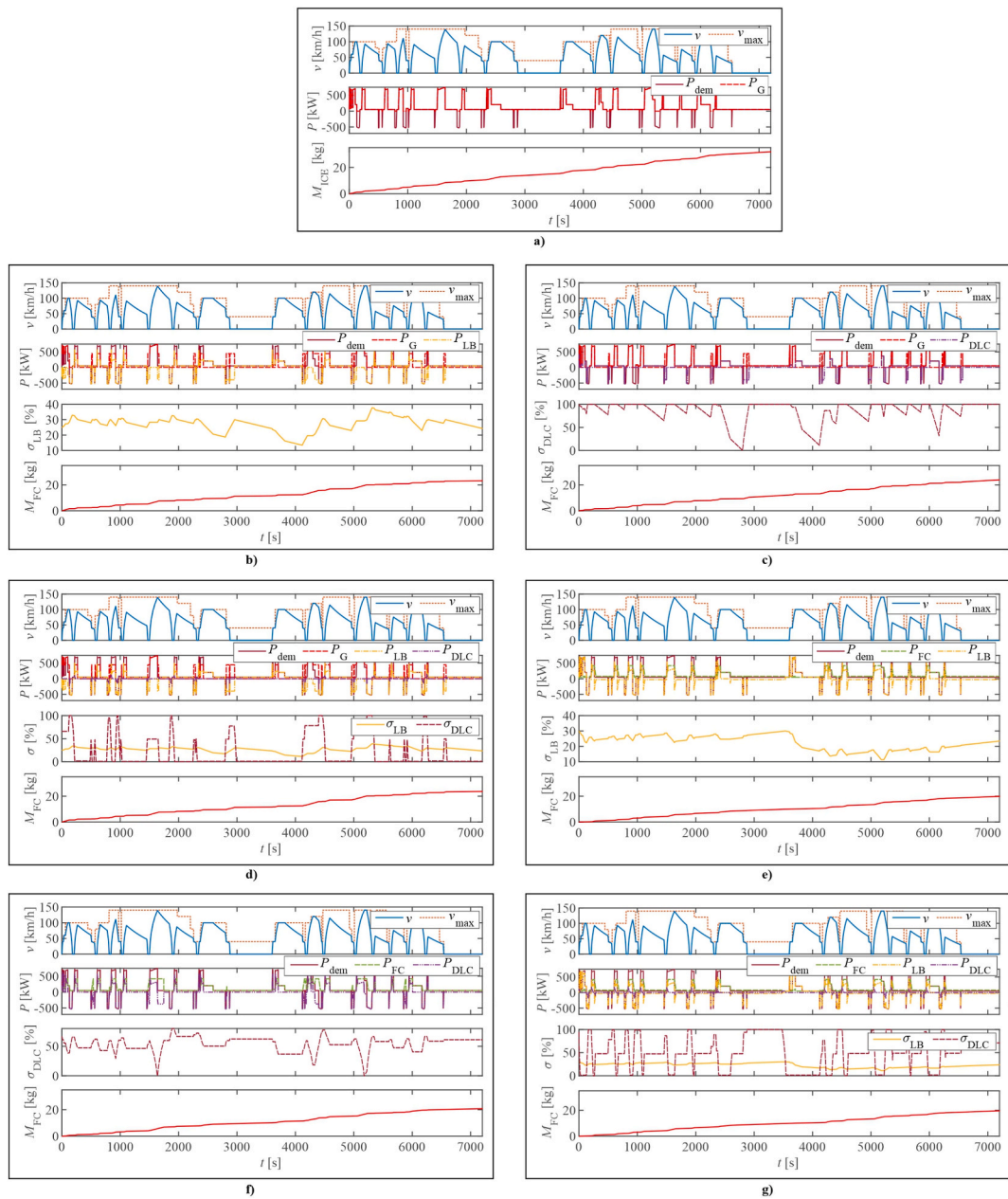
Fig. 11. Simulation results for alternative propulsion systems complying with the maximum range requirement: (a) standard (non-hybrid); internal combustion engine-based hybrids with (b) lithium-ion battery, (c) double-layer capacitor, and (d) hybrid energy storage system; fuel cell-based hybrids with (e) lithium-ion battery, (f) double-layer capacitor, and (g) hybrid energy storage system.

Table 6
Estimated hydrogen consumption per round trip for alternative system configurations complying with the maximum range requirement.

Configuration	Prime mover	Energy storage system	Hydrogen consumption [kg]
1	Internal combustion engine	–	31.87
2	Internal combustion engine	Lithium-ion battery	22.85
3	Internal combustion engine	Double-layer capacitor	24.95
4	Internal combustion engine	Hybrid energy storage system	23.28
5	Fuel cell	Lithium-ion battery	19.80
6	Fuel cell	Double-layer capacitor	21.02
7	Fuel cell	Hybrid energy storage system	19.83

Table 7

Characteristics and estimated hydrogen consumption for alternative system configurations complying with weight and volumetric space constraints.

	Configuration						
	1	2	3	4	5	6	7
Number of hydrogen fuel cylinders	23	10	9	9	23	8	22
Hydrogen consumption per trip [kg]	31.06	22.13	24.01	22.67	19.80	20.32	19.78
Fuel savings compared to the full range [%]	2.54	3.15	3.77	2.62	0.00	3.33	0.25
Vehicle range (number of round trips)	5	3	2	3	9	3	8

Characteristics and estimated hydrogen consumption for adjusted vehicle configurations are summarized in Table 7. Due to reduced vehicle weight, affecting the acceleration and braking performance, additional fuel savings are obtained. Compared to the previous scenario, these savings range between 0.25% for FCMU with HESS up to 3.77% for ICE-based hybrid with DLC. At the same time, vehicle range is reduced to 2 up to 8 round trips, depending on the configuration. Again, FCMU with LB and HESS demonstrated the highest fuel economy, with a slightly lower consumption of HESS-equipped vehicle in this case (0.1%).

4.5.3. Preliminary validation of energy use

Available historical data on actual fuel consumption provided by the railway undertaking for the Dutch Northern lines shows an average annual consumption of diesel per vehicle-distance travelled of 0.94 l/km and 0.95 l/km, in 2019 and 2020, respectively. This is a 3–4% lower diesel consumption compared to our estimations for a standard diesel-electric vehicle, i.e., a total consumption of 87.78 kg (106.4 l) for a round trip, giving an average consumption of 0.98 l/km. This difference can be attributed to various factors, including the variation in duty cycles linked to different lines in the network, passengers load and auxiliary systems consumption over different seasons and time of the day. In addition, our estimations are based on the assumption that all auxiliary systems are active during layover times, while in reality this is not always the case.

Furthermore, the onboard system used for train drivers training that registers fuel consumption during each trip (excluding the layover time) showed an average diesel fuel consumption for GTW 2/6 DEMUs in a range 0.66–0.86 l/km and 0.70–0.92 l/km for the Leeuwarden-Groningen and Groningen-Leeuwarden directions, respectively. With the layover time omitted, our estimations are within
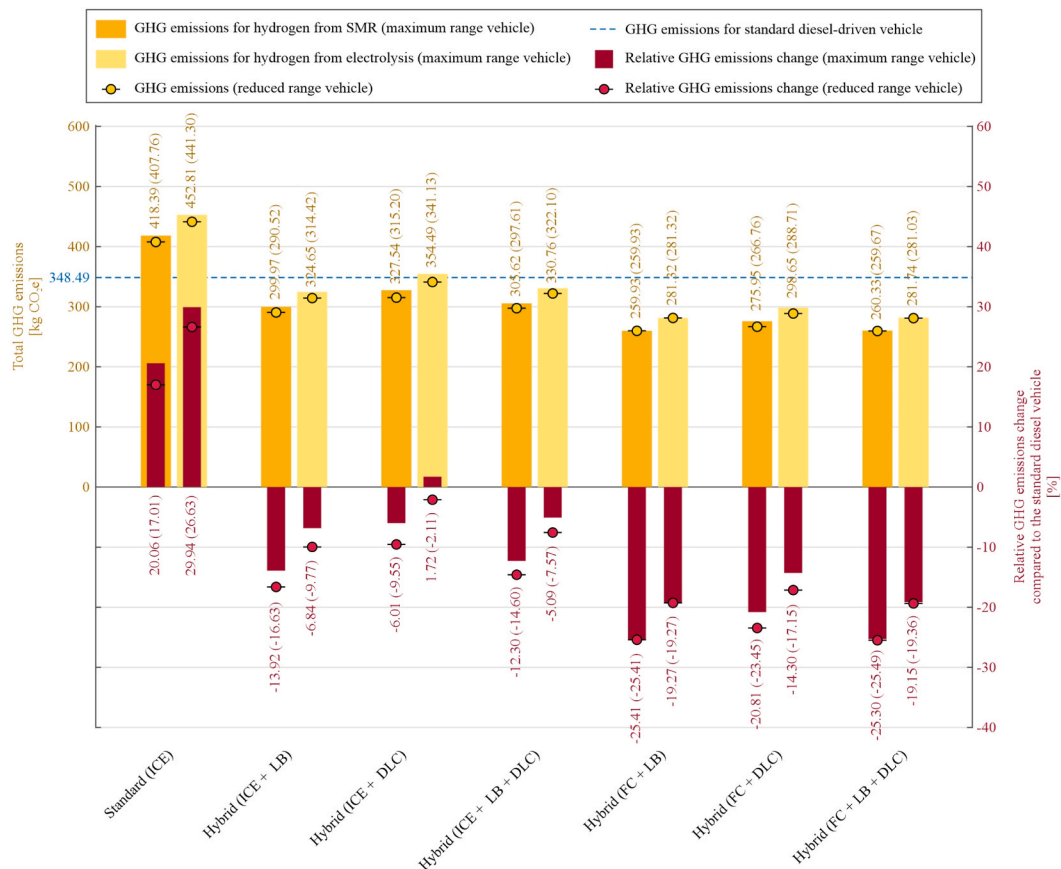
Fig. 12. Estimated greenhouse gas (GHG) emissions and relative GHG emissions change compared to the standard diesel vehicle.

the given range for both directions, i.e., 36.86 kg (0.83 l/km) for the Leeuwarden-Groningen trip, and 40.65 kg (0.91 l/km) for the Groningen-Leeuwarden trip.

In addition, although there are numerous factors affecting the estimates, including the observed technology, size, and operation context, the model estimations are compared to the scientific findings in the literature that considers similar use cases, i.e., regional railway transport and multiple-unit vehicles. Our estimations on fuel consumption for a standard DEMU, and relative savings for ICE-based hybrid powertrains compared to the standard vehicle, are close or within the range of the estimations in scientific studies that considered various geographical contexts, technologies and test conditions, c. f., Lanneluc et al. (2017); Leska et al. (2017); Meinert et al. (2015b); Poline et al. (2019); Schmid et al. (2017). Regarding FC-based systems, it can be noted that our estimations on hydrogen consumption of 0.37–0.39 kg/km, depending on the ESS configuration, are similar to, or within the range of the estimations found in studies on regional hybrid trains, c. f., Din and Hillmansen (2018); Hoffrichter et al. (2016); Peng et al. (2020a).

4.5.4. Greenhouse gas emissions

Although hydrogen as fuel leads to zero direct GHG emissions, its overall environmental impact heavily depends on its production pathway. Therefore, it is important to adopt the so-called "well-to-wheel" approach, where the emissions from upstream processes related to hydrogen production are accounted. This allows for a plausible and fair comparison of GHG emissions linked to the alternative hydrogen-based scenarios and the benchmark diesel-driven vehicle. To assess the influence of hydrogen production, we include two common hydrogen production pathways – steam methane reforming (SMR) and electrolysis of water. Corresponding emission factors are derived from the latest JEC report (JRC, 2020b), and represent the amount of GHG emissions expressed in kilograms of CO_2-equivalents per kilogram of fuel expended (kgCO_2e/kg). Considered production of hydrogen from SMR includes typical EU natural gas supply transported to EU by pipeline (1900 km), distributed inside the EU (500 km) through high-pressure trunk lines and a low-pressure grid, small scale reforming at a retail site, and hydrogen compression to 88 MPa, with a corresponding emission factor of 13.128 kgCO_2e/kg. The electrolysis scenario considers hydrogen produced from a central electrolysis with medium voltage electricity, hydrogen transport by pipeline and compression to 88 MPa. To account for future trends, the electricity used is based on predicted EU-mix electricity supply relevant for 2030, resulting in a hydrogen emission factor of 14.208 kgCO_2e/kg. Electrolysis using electricity produced solely from renewables, e.g., wind energy, is not considered, as it would practically lead to net-zero emissions for all scenarios. Furthermore, it is expected that such a production process leads to a significantly higher price of hydrogen compared to the SMR, with a current hydrogen price of 2 Euros per kilogram (Klebsch et al., 2019). The baseline scenario considers diesel fuel produced from crude oil from typical EU supply transported by sea, refined in EU (marginal production), with typical EU distribution and retail, resulting in a well-to-wheel emission factor of 3.970 kgCO_2e/kg.

Overall GHG emissions for the two production scenarios are obtained by multiplying the estimated hydrogen consumption given in Tables 6 and 7 with corresponding emission factors. The results are then compared to the baseline estimate for a diesel-driven vehicle in terms of relative change in GHG emissions (Fig. 12). As noted, conversion to a standard hydrogen ICE-based configuration would potentially lead to a significant increase of GHG emissions compared to diesel baseline (~17–30%). Another configuration that showed an increase of 1.72% compared to the baseline is the maximum range of ICE-based hybrid with DLC. A reduction of GHG emissions is achieved in all remaining scenarios, with the highest savings reached by FCMU with LB or HESS, as the most fuel-efficient configurations.

5. Conclusions

This paper presented a comparative assessment of hydrogen-powered propulsion systems with an internal combustion engine or fuel cells as the prime mover, hybridized with different energy storage system configurations, based on lithium-ion batteries and double-layer capacitors. The analysis encompassed the technology identification, design, modelling and assessment of alternative powertrains, with respect to the particular case-related constraints imposed by the infrastructure, technical and operational requirements. Focusing on the regional railways in the Northern Netherlands, we investigated the possibilities of converting a conventional benchmark vehicle used in current operations, and provided a simulation-based assessment in terms of overall hydrogen consumption.

According to the results, the highest fuel-saving potential was found for the fuel cell-based hybrid propulsion systems with lithium-ion battery or a hybrid energy storage system, that combines both energy storage system technologies, while at the same time complying with the volumetric space and weight limitations. Additionally, the previous two configurations demonstrated the highest greenhouse gas emissions reduction compared to the benchmark diesel-driven vehicle, i.e., between 25.3 and 25.5% for hydrogen produced by steam methane reforming, and between 19.2 and 19.4%, if hydrogen obtained through electrolysis of water is used.

Overall, our results indicate promising potential benefits from adopting hydrogen-based technology and provide decision-makers with valuable input in defining a roadmap for the railway transport development in the northern Netherlands. Future research efforts will include the application of the proposed method to the remaining lines and rolling stock in the network while addressing limitations of the present study resulting primarily from a wide range of data sources used and a degree of variability in parameters and assumptions adopted. Regarding the variability of parameters, one of the main challenges in practical implementation is the consideration of real-life phenomena such as fuel cell deterioration and battery degradation due to aging, which can affect the system's performance. Another system engineering challenge is incorporating safety requirements and vehicle/components geometrics, which require more detailed analyses including, for instance, developing detailed 3D CAD models.

The presented research is part of a wider-scope project realized in collaboration with Arriva, aiming to investigate the overall environemental impacts from novel technology adoption and possibilities to reduce the carbon footprint from trains operation. In this

context, extensions of the present research will include further investigation of alternative fuels and upstream processes related to their production through a detailed well-to-wheel analysis. The environmental impacts of technology production and vehicle retrofit will be evaluated by a life cycle assessment approach, as introduced by Jones et al. (2017). Furthermore, a comprehensive life cycle costs analysis, based on Zhang et al. (2016) will be realized to assess the fixed investment costs for both onboard hydrogen technologies and stationary infrastructure required for refueling. As shown by Logan et al. (2020), railways should also be observed in a wider transport system context. Therefore, future research could consider network-wide operational measures (Dunbar et al., 2017), or policy interventions with the potential to increase the modal shift from individual road transport to rail.

The methodology provided in this paper offers numerous possibilities for other railway market segments. The high level of generality and ability to capture main technology, infrastructure and operation characteristics allow for its application in urban and freight rail transport, as well as in different contexts of regional railway transport, where, for instance, different vehicle features, speed limits and/or track geometry profiles determine corresponding duty cycles and the final outcomes of the analysis. Thus, our findings provide decision-makers with a valuable tool in assessing future investments planning, including the identification of suitable powertrain technology and potential benefits in terms of fuel economy and reduction of emissions.

Acknowledgment

References

ABB, 2018. BORDLINE® CC750 DE. For diesel-electric regional trains (DMU). Available online: https://library.e.abb.com/public/1b988f5784ff4676b460b46553050347/BORDLINE CC750 DE M U RevC EN.pdf. (Accessed 21 March 2022) (accessed on.

Akal, D., Öztuna, S., Büyükakın, M.K., 2020. A review of hydrogen usage in internal combustion engines (gasoline-Lpg-diesel) from combustion performance aspect. Int. J. Hydrogen Energy 45, 35257–35268. https://doi.org/10.1016/j.ijhydene.2020.02.001.

Alstom, 2020. Alstom's Hydrogen Train Enters Regular Passenger Service in Austria. Alstom Press Release. Available online: https://www.alstom.com/press-releases-news/2020/9/alstoms-hydrogen-train-enters-regular-passenger-service-austria. (Accessed 15 April 2021). accessed on.

Bagotsky, V.S., Skundin, A.M., Volfkovich, Y.M., 2015. Electrochemical power sources: batteries. In: Fuel Cells, and Supercapacitors. John Wiley & Sons,Inc., Hoboken, New Jersey.

Ballard, 2021. FCmove. Available online: https://www.ballard.com/about-ballard/publication_library/product-specification-sheets/fcmovetm-spec-sheet. (Accessed 4 April 2021). accessed on.

Barbir, B., 2013. PEM Fuel Cells: Theory and Practice, second ed. Elsevier Inc. https://doi.org/10.1016/C2011-0-06706-6.

Barbosa, F.C., 2019. Fuel cell rail technology review: a tool for an autonomous rail electrifying strategy. In: 2019 Joint Rail Conference. American Society of Mechanical Engineers. https://doi.org/10.1115/JRC2019-1223.

Beatrice, C., Rispoli, N., Di Blasio, G., Patrianakos, G., Kostoglou, M., Konstandopoulos, A., Imren, A., Denbratt, I., Palacin, R., 2013. Emission reduction technologies for the future low emission rail diesel engines: EGR vs SCR. In: SAE Technical Papers. https://doi.org/10.4271/2013-24-0087.

Brünger, O., Dahlhaus, E., 2014. Running time estimation. In: Hansen, I.A., Pachl, J. (Eds.), Railway Timetabling & Operations. Eurailpress, Hamburg, pp. 65–89.

Calvert, C., Allan, J., Amor, P., Hillmansen, S., Roberts, C., Weston, P., 2021. Concept development and testing of the UK's first hydrogen-hybrid train (HydroFLEX). Railw. Eng. Sci. 29, 248–257. https://doi.org/10.1007/s40534-021-00256-9.

Carrette, L., Friedrich, K.A., Stimming, U., 2001. Fuel cells - fundamentals and applications. Fuel Cell. 1, 5–39. https://doi.org/10.1002/1615-6854(200105)1:1<5::AID-FUCE5>3.0.CO;2-G.

Chen, X., Wang, Y., Zhao, Y., Zhou, Y., 2016. A study of double functions and load matching of a phosphoric acid fuel cell/heat-driven refrigerator hybrid system. Energy 101, 359–365. https://doi.org/10.1016/j.energy.2016.02.029.

Davis, W.J., 1926. The tractive resistance of electric locomotives and cars. Gen. Electr. Rev. 29, 685–707.

Deutz, 2021. DEUTZ hydrogen engine ready for the market. Available online: https://www.deutz.com/en/media/press-releases/deutz-hydrogen-engine-ready-for-the-market. (Accessed 6 September 2021) (accessed on.

Din, T., Hillmansen, S., 2018. Energy consumption and carbon dioxide emissions analysis for a concept design of a hydrogen hybrid railway vehicle. IET Electr. Syst. Transp. 8, 112–121. https://doi.org/10.1049/iet-est.2017.0049.

Dincer, I., Zamfirescu, C., 2016. A review of novel energy options for clean rail applications. J. Nat. Gas Sci. Eng. 28, 461–478. https://doi.org/10.1016/j.jngse.2015.12.007.

Dittus, H., Hülsebusch, D., Ungethüm, J., 2011. Reducing DMU fuel consumption by means of hybrid energy storage. Eur. Transp. Res. Rev. 3, 149–159. https://doi.org/10.1007/s12544-011-0053-6.

Dunbar, R., Roberts, C., Zhao, N., 2017. A tool for the rapid selection of a railway signalling strategy to implement train control optimisation for energy saving. J. Rail Transp. Plan. Manag. 7, 224–244. https://doi.org/10.1016/j.jrtpm.2017.09.002.

Fotouhi, A., Auger, D.J., Propp, K., Longo, S., Wild, M., 2016. A review on electric vehicle battery modelling: from Lithium-ion toward Lithium–Sulphur. Renew. Sustain. Energy Rev. 56, 1008–1021. https://doi.org/10.1016/j.rser.2015.12.009.

Fragiacomo, P., Piraino, F., 2021. Vehicle-to-grid application with hydrogen-based tram. Energy Convers. Manag. 250, 114915 https://doi.org/10.1016/j.enconman.2021.114915.

Fragiacomo, P., Piraino, F., 2019. Fuel cell hybrid powertrains for use in Southern Italian railways. Int. J. Hydrogen Energy 44, 27930–27946. https://doi.org/10.1016/j.ijhydene.2019.09.005.

FuelCellWorks, 2020. Siemens Mireo Plus H fuel cell hydrogen train - the middle distance champion. Available online: https://fuelcellworks.com/news/siemens-mireo-plus-h-fuel-cell-hydrogen-train-the-middle-distance-champion/. (Accessed 5 April 2021) (accessed on.

Gallucci, M., 2019. Hydrogen trains roll into service: a new hybrid locomotive signals a growing push for zero-emission rail technologies - [News]. IEEE Spectr 56, 6–7. https://doi.org/10.1109/MSPEC.2019.8784110.

Garcia, P., Fernandez, L.M., Garcia, C.A., Jurado, F., 2010. Energy management system of fuel-cell-battery hybrid tramway. IEEE Trans. Ind. Electron. 57, 4013–4023. https://doi.org/10.1109/TIE.2009.2034173.

Ghaviha, N., Bohlin, M., Holmberg, C., Dahlquist, E., 2019. Speed profile optimization of catenary-free electric trains with lithium-ion batteries. J. Mod. Transp. 27, 153–168. https://doi.org/10.1007/s40534-018-0181-y.

Ghaviha, N., Campillo, J., Bohlin, M., Dahlquist, E., 2017. Review of application of energy storage devices in railway transportation. Energy Proc. 105, 4561–4568. https://doi.org/10.1016/j.egypro.2017.03.980.

Giro Batalla, R., Feenstra, M., 2012. Energy Consumption in GTW DMU Trains - ECO Driving. Project statement, Arriva Nederland.

González-Gil, A., Palacin, R., Batty, P., 2013. Sustainable urban rail systems: strategies and technologies for optimal management of regenerative braking energy. Energy Convers. Manag. 75, 374–388. https://doi.org/10.1016/j.enconman.2013.06.039.

Guo, Y., Dai, X., Jermsittiparsert, K., Razmjooy, N., 2020. An optimal configuration for a battery and PEM fuel cell-based hybrid energy system using developed Krill herd optimization algorithm for locomotive application. Energy Rep. 6, 885–894. https://doi.org/10.1016/j.egyr.2020.04.012.

Han, Y., Cao, N., Hong, Z., Li, Q., Chen, W., 2016. Experimental study on energy management strategy for fuel cell hybrid tramway. In: 2016 IEEE Vehicle Power and Propulsion Conference (VPPC). IEEE, pp. 1–6. https://doi.org/10.1109/VPPC.2016.7791686.

Han, Y., Li, Q., Wang, T., Chen, W., Ma, L., 2018. Multisource coordination energy management strategy based on SOC consensus for a PEMFC–battery–supercapacitor hybrid tramway. IEEE Trans. Veh. Technol. 67, 296–305. https://doi.org/10.1109/TVT.2017.2747135.

Han, Y., Meng, X., Zhang, G., Li, Q., Chen, W., 2017. An energy management system based on hierarchical control and state machine for the PEMFC-battery hybrid tramway. In: 2017 IEEE Transportation Electrification Conference and Expo, Asia-Pacific (ITEC Asia-Pacific). IEEE, pp. 1–5. https://doi.org/10.1109/ITEC-AP.2017.8080856.

Hoffrichter, A., Miller, A.R., Hillmansen, S., Roberts, C., 2012. Well-to-wheel analysis for electric, diesel and hydrogen traction for railways. Transport. Res. Transport Environ. 17, 28–34. https://doi.org/10.1016/j.trd.2011.09.002.

Hoffrichter, A., Roberts, C., Hillmansen, S., 2016. Conceptual propulsion system design for a hydrogen-powered regional train. IET Electr. Syst. Transp. 6, 56–66. https://doi.org/10.1049/iet-est.2014.0049.

Hong, Z., Li, Q., Han, Y., Shang, W., Zhu, Y., Chen, W., 2018. An energy management strategy based on dynamic power factor for fuel cell/battery hybrid locomotive. Int. J. Hydrogen Energy 43, 3261–3272. https://doi.org/10.1016/j.ijhydene.2017.12.117.

Huerlimann, D., Nash, A., 2003. Open track-simulation of Railway Networks user manual version 1.3.

IRJ, 2019. Zillertalbahn hydrogen train design revealed. Int. Railw. J. Available online: https://www.railjournal.com/fleet/zillertalbahnhydrogen-train-design-revealed/. (Accessed 5 April 2021) accessed on.

Jones, H., Moura, F., Domingos, T., 2017. Life cycle assessment of high-speed rail: a case study in Portugal. Int. J. Life Cycle Assess. 22, 410–422. https://doi.org/10.1007/s11367-016-1177-7.

JRC, 2020a. JEC Well-To-Wheels report v5. Well-to-Wheels analysis of future automotive fuels and powertrains in the European context. Luxembourg. https://doi.org/10.2760/100379.

JRC, 2020b. JEC Well-to-Tank report v5. Well-to-Wheels analysis of future automotive fuels and powertrains in the European context. Luxembourg. https://doi.org/10.2760/959137.

Kapetanović, M., Núñez, A., van Oort, N., Goverde, R.M.P., 2021a. Reducing fuel consumption and related emissions through optimal sizing of energy storage systems for diesel-electric trains. Appl. Energy 294, 117018. https://doi.org/10.1016/j.apenergy.2021.117018.

Kapetanović, M., Vajihi, M., Goverde, R.M.P., 2021b. Analysis of hybrid and plug-in hybrid alternative propulsion systems for regional diesel-electric multiple unit trains. Energies 14, 5920. https://doi.org/10.3390/en14185920.

Klebsch, W., Guckes, N., Heininger, P., 2020. Evaluation of climate-neutral alternatives to diesel multiple units: economic viability assessment based on the example of the 〉Düren network〈. Frankf. Main.

Klebsch, W., Heininger, P., Martin, J., 2019. Alternatives to diesel multiple units in regional passenger rail transport: assessment of systemic potential. Frankf. Main.

Knorr, H., Held, W., Prumm, W., Rudiger, H., 1998. The MAN hydrogen propulsion system for city buses. Int. J. Hydrogen Energy 23, 201–208. https://doi.org/10.1016/S0360-3199(97)00045-1.

Kordesch, K., Hacker, V., Gsellmann, J., Cifrain, M., Faleschini, G., Enzinger, P., Fankhauser, R., Ortner, M., Muhr, M., Aronson, R.R., 2000. Alkaline fuel cells applications. J. Power Sources 86, 162–165. https://doi.org/10.1016/S0378-7753(99)00429-2.

Krastev, I., Tricoli, P., 2022. Boost multilevel cascade inverter for hydrogen fuel cell light railway vehicles. IEEE Trans. Ind. Electron. 69, 7837–7847. https://doi.org/10.1109/TIE.2021.3105992.

Lanneluc, C., Pouget, J., Poline, M., Chauvet, F., Gerbaud, L., 2017. Optimal energy management of a hybrid train: focus on saving braking energy. In: 2017 IEEE Vehicle Power and Propulsion Conference (VPPC). IEEE, pp. 1–6. https://doi.org/10.1109/VPPC.2017.8330927.

Leska, M., Aschemann, H., Melzer, M., Meinert, M., 2017. Comparative calculation of the fuel-optimal operating strategy for diesel hybrid railway vehicles. Int. J. Appl. Math. Comput. Sci. 27, 323–336. https://doi.org/10.1515/amcs-2017-0023.

Leska, M., Gruning, T., Aschemann, H., Rauh, A., 2013. Optimal trajectory planning for standard and hybrid railway vehicles with a hydro-mechanic transmission. In: 2013 Eur. Control Conf. ECC 2013 4550–4555. https://doi.org/10.23919/ecc.2013.6669576.

Leska, M., Gruning, T., Aschemann, H., Rauh, A., 2012. Optimization of the longitudinal dynamics of parallel hybrid railway vehicles. Proc. IEEE Int. Conf. Control Appl. 202–207. https://doi.org/10.1109/CCA.2012.6402436.

Li, H., Ravey, A., N'Diaye, A., Djerdir, A., 2019. Online adaptive equivalent consumption minimization strategy for fuel cell hybrid electric vehicle considering power sources degradation. Energy Convers. Manag. 192, 133–149. https://doi.org/10.1016/j.enconman.2019.03.090.

Li, Minggao, Li, Ming, Han, G., Liu, N., Zhang, Q., Wang, Y., 2018. Optimization analysis of the energy management strategy of the new energy hybrid 100% low-floor tramcar using a genetic algorithm. Appl. Sci. 8, 1144. https://doi.org/10.3390/app8071144.

Li, Q., Yang, H., Han, Y., Li, M., Chen, W., 2016. A state machine strategy based on droop control for an energy management system of PEMFC-battery-supercapacitor hybrid tramway. Int. J. Hydrogen Energy 41, 16148–16159. https://doi.org/10.1016/j.ijhydene.2016.04.254.

Liu, J., Wu, X., Li, H., Qi, L., 2020. An optimal method of the energy consumption for fuel cell hybrid tram. Int. J. Hydrogen Energy 45, 20304–20311. https://doi.org/10.1016/j.ijhydene.2019.12.135.

Logan, K.G., Nelson, J.D., McLellan, B.C., Hastings, A., 2020. Electric and hydrogen rail: potential contribution to net zero in the UK. Transport. Res. Transport Environ. 87, 102523 https://doi.org/10.1016/j.trd.2020.102523.

Luxfer, 2020a. Hydrogen cylinders for alternative fuel trains. Available online: https://www.luxfercylinders.com/support/hydrogen-cylinders-for-alternative-fuel-trains/alternative-fuel. (Accessed 3 July 2021). accessed on.

Luxfer, 2020b. Specification data: G-stor H2 alternative fuel cylinders. Available online: https://www.luxfercylinders.com/support/luxfer-g-stor-h2-spec-sheet. (Accessed 5 July 2021). accessed on.

Madovi, O., Hoffrichter, A., Little, N., Foster, S.N., Isaac, R., 2021. Feasibility of hydrogen fuel cell technology for railway intercity services: a case study for the Piedmont in North Carolina. Railw. Eng. Sci. 29, 258–270. https://doi.org/10.1007/s40534-021-00249-8.

Maleki, A., Rosen, M.A., 2017. Design of a cost-effective on-grid hybrid wind–hydrogen based CHP system using a modified heuristic approach. Int. J. Hydrogen Energy 42, 15973–15989. https://doi.org/10.1016/j.ijhydene.2017.01.169.

Man, 2020. MAN Presents Zero-Emission Roadmap. Press Release. MAN Truck & Bus. Available online: https://press.mantruckandbus.com/corporate/man-presents-zero-emission-roadmap/. (Accessed 7 September 2021). accessed on.

Marin, G.D., Naterer, G.F., Gabriel, K., 2010. Rail transportation by hydrogen vs. electrification – case study for Ontario, Canada, II: energy supply and distribution. Int. J. Hydrogen Energy 35, 6097–6107. https://doi.org/10.1016/j.ijhydene.2010.03.095.

Maxwell, 2021. 125 volt transportation module. Available online: https://www.maxwell.com/products/ultracapacitors/125v-tran-modules#. (Accessed 4 June 2021) https://www.maxwell.com/products/ultracapacitors/125v-tran-modules#. accessed on.

Meinert, M., Melzer, M., Kamburow, C., Palacin, R., Leska, M., Aschemann, H., 2015a. Benefits of hybridisation of diesel driven rail vehicles: energy management strategies and life-cycle costs appraisal. Appl. Energy 157, 897–904. https://doi.org/10.1016/j.apenergy.2015.05.051.

Meinert, M., Prenleloup, P., Schmid, S., Palacin, R., 2015b. Energy storage technologies and hybrid architectures for specific diesel-driven rail duty cycles: design and system integration aspects. Appl. Energy 157, 619–629. https://doi.org/10.1016/j.apenergy.2015.05.015.

Miller, A.R., Hess, K.S., Barnes, D.L., Erickson, T.L., 2007. System design of a large fuel cell hybrid locomotive. J. Power Sources 173, 935–942. https://doi.org/10.1016/j.jpowsour.2007.08.045.

Mueller, F., Guerster, M., Obrenovic, N., Bierlaire, M., 2020. Can regional railway become emission-free with recently announced vehicles? - a case study of Bavaria. Eur. J. Transport Infrastruct. Res. 20, 286–305. https://doi.org/10.18757/ejtir.2020.20.4.5315.

Ogawa, T., Yoshihara, H., Wakao, S., Kondo, K., Kondo, M., 2007. Energy consumption analysis of FC-EDLC hybrid railway vehicle by dynamic programming. In: 2007 European Conference on Power Electronics and Applications. IEEE, pp. 1–8. https://doi.org/10.1109/EPE.2007.4417520.

Paukert, H., 2011. CleanER-D Deliverable 7.2.1: Detailed Specification: Parameters Definition.

Peng, F., Chen, W., Liu, Z., Li, Q., Dai, C., 2014. System integration of China's first proton exchange membrane fuel cell locomotive. Int. J. Hydrogen Energy 39, 13886–13893. https://doi.org/10.1016/j.ijhydene.2014.01.166.

Peng, F., Zhao, Y., Chen, T., Zhang, X., Chen, W., Zhou, D., Li, Q., 2018. Development of robust suboptimal real-time power sharing strategy for modern fuel cell based hybrid tramways considering operational uncertainties and performance degradation. Appl. Energy 226, 503–521. https://doi.org/10.1016/j.apenergy.2018.05.092.

Peng, H., Li, J., Löwenstein, L., Hameyer, K., 2020a. A scalable, causal, adaptive energy management strategy based on optimal control theory for a fuel cell hybrid railway vehicle. Appl. Energy 267, 114987. https://doi.org/10.1016/j.apenergy.2020.114987.

Peng, H., Li, J., Thul, A., Deng, K., Ünlübayir, C., Löwenstein, L., Hameyer, K., 2020b. A scalable, causal, adaptive rule-based energy management for fuel cell hybrid railway vehicles learned from results of dynamic programming. eTransportation 4, 100057. https://doi.org/10.1016/j.etran.2020.100057.

Pesaran, A., Kim, G.-H., Gonder, J., 2005. PEM Fuel Cell Freeze and Rapid Startup Investigation. Milestone Report NREL/MP-540-38760, Golden, Colorado.

Piraino, F., Fragiacomo, P., 2020. A multi-method control strategy for numerically testing a fuel cell-battery-supercapacitor tramway. Energy Convers. Manag. 225, 113481 https://doi.org/10.1016/j.enconman.2020.113481.

Poline, M., Gerbaud, L., Pouget, J., Chauvet, F., 2019. Simultaneous optimization of sizing and energy management — application to hybrid train. Math. Comput. Simulat. 158, 355–374. https://doi.org/10.1016/j.matcom.2018.09.021.

Pourabdollah, M., Murgovski, N., Grauers, A., Egardt, B., 2013. Optimal sizing of a parallel PHEV powertrain. IEEE Trans. Veh. Technol. 62, 2469–2480. https://doi.org/10.1109/TVT.2013.2240326.

Pröhl, L., 2017a. OPEUS Deliverable DO2.1 - OPEUS Simulation Methodology. EU-project OPEUS (S2R-OC-CCA-02-2015).

Pröhl, L., 2017b. OPEUS Deliverable DO2.2 - OPEUS Simulation Tool. EU-project OPEUS (S2R-OC-CCA-02-2015).

Prohl, L., Aschemann, H., 2019. Grey Wolf optimisation of an operating strategy for energy storage systems in electrically driven railway vehicles. In: 2019 18th Eur. Control Conf. ECC 2019 1908–1913. https://doi.org/10.23919/ECC.2019.8795720.

RailTech, 2020. Report from a night-time trial on a hydrogen train. Available online: https://www.railtech.com/rolling-stock/2020/03/07/report-from-a-night-time-trial-on-a-hydrogen-train/. (Accessed 2 February 2022). accessed on.

Sarma, U., Ganguly, S., 2020. Design optimisation for component sizing using multi-objective particle swarm optimisation and control of PEM fuel cell-battery hybrid energy system for locomotive application. IET Electr. Syst. Transp. 10, 52–61. https://doi.org/10.1049/iet-est.2018.5053.

SAFT, UNEW, 2017. OPEUS Deliverable D6.1 - Innovative Technologies Outlook Update. Shift2Rail. EUproject OPEUS (S2R-OC-CCA-02-2015).

Sarma, U., Ganguly, S., 2018. Determination of the component sizing for the PEM fuel cell-battery hybrid energy system for locomotive application using particle swarm optimization. J. Energy Storage 19, 247–259. https://doi.org/10.1016/j.est.2018.08.008.

Schmid, S., Ebrahimi, K., Pezouvanis, A., Commerell, W., 2017. Model-based comparison of hybrid propulsion systems for railway diesel multiple units. Int. J. Rail Transp. 6, 16–37. https://doi.org/10.1080/23248378.2017.1390790.

Siddiqui, O., Dincer, I., 2019. A review on fuel cell-based locomotive powering options for sustainable transportation. Arabian J. Sci. Eng. 44, 677–693. https://doi.org/10.1007/s13369-018-3607-2.

Silvas, E., Hofman, T., Murgovski, N., Etman, P., Steinbuch, M., 2016. Review of optimization strategies for system-level design in hybrid electric vehicles. IEEE Trans. Veh. Technol. 66 https://doi.org/10.1109/TVT.2016.2547897, 1–1.

Sopian, K., Wan Daud, W.R., 2006. Challenges and future developments in proton exchange membrane fuel cells. Renew. Energy 31, 719–727. https://doi.org/10.1016/j.renene.2005.09.003.

Spiryagin, M., Cole, C., Sun, Y.Q., McClanachan, M., Spiryagin, V., McSweeney, T., 2014. Design and Simulation of Rail Vehicles, first ed. Taylor & Francis Group, LLC.

Stadler, 2021. Overview of references. Available online: https://www.stadlerrail.com/en/references/overview-references/. (Accessed 9 September 2021). accessed on.

Stadler, 2005. GTW DMU-2 2/6 and GTW 2/8 low-floor for Arriva, Netherlands. Available online: https://www.stadlerrail.com/media/pdf/garr1008e.pdf. (Accessed 4 March 2021). accessed on.

Sun, Y., Anwar, M., Hassan, N.M.S., Spiryagin, M., Cole, C., 2021. A review of hydrogen technologies and engineering solutions for railway vehicle design and operations. Railw. Eng. Sci. 29, 212–232. https://doi.org/10.1007/s40534-021-00257-8.

Takami, N., Inagaki, H., Tatebayashi, Y., Saruwatari, H., Honda, K., Egusa, S., 2013. High-power and long-life lithium-ion batteries using lithium titanium oxide anode for automotive and stationary power applications. J. Power Sources 244, 469–475. https://doi.org/10.1016/j.jpowsour.2012.11.055.

Tao, S., Chen, W., Gan, R., Li, L., Zhang, G., Han, Y., Li, Q., 2021. Energy management strategy based on dynamic programming with durability extension for fuel cell hybrid tramway. Railw. Eng. Sci. 29, 299–313. https://doi.org/10.1007/s40534-021-00247-w.

Torreglosa, J.P., Jurado, F., García, P., Fernández, L.M., 2011a. Hybrid fuel cell and battery tramway control based on an equivalent consumption minimization strategy. Control Eng. Pract. 19, 1182–1194. https://doi.org/10.1016/j.conengprac.2011.06.008.

Torreglosa, J.P., Jurado, F., García, P., Fernández, L.M., 2011b. Application of cascade and fuzzy logic based control in a model of a fuel-cell hybrid tramway. Eng. Appl. Artif. Intell. 24, 1–11. https://doi.org/10.1016/j.engappai.2010.08.009.

Toshiba, 2021. SCiB^{TM} Rechargeable battery. Available online: https://www.global.toshiba/ww/products-solutions/battery/scib.html. (Accessed 2 February 2021). accessed on.

UIC, CER, 2012. Moving towards sustainable mobility: a strategy for 2030 and beyond for the European railway sector. Paris.

US Department of Energy, 2021. Comparison of fuel cell technologies. Available online: https://www.energy.gov/eere/fuelcells/comparison-fuel-cell-technologies. (Accessed 12 May 2021). accessed on.

Vazquez, S., Lukic, S.M., Galvan, E., Franquelo, L.G., Carrasco, J.M., 2010. Energy storage systems for transport and grid applications. IEEE Trans. Ind. Electron. 57, 3881–3895. https://doi.org/10.1109/TIE.2010.2076414.

Wang, Y., Chen, K.S., Mishler, J., Cho, S.C., Adroher, X.C., 2011. A review of polymer electrolyte membrane fuel cells: technology, applications, and needs on fundamental research. Appl. Energy 88, 981–1007. https://doi.org/10.1016/j.apenergy.2010.09.030.

Washing, E.M., Pulugurtha, S.S., 2016. Energy demand and emission production comparison of electric, hydrogen and hydrogen-hybrid light rail trains. Int. J. Rail Transp. 4, 55–70. https://doi.org/10.1080/23248378.2015.1086554.

Xu, L., Li, J., Ouyang, M., 2015. Energy flow modeling and real-time control design basing on mean values for maximizing driving mileage of a fuel cell bus. Int. J. Hydrogen Energy 40, 15052–15066. https://doi.org/10.1016/j.ijhydene.2015.08.104.

Yan, Y., Huang, W., Liu, J., Li, Q., Chen, W., 2019. The control strategy of fuel cell hybrid tram based on state machine control. In: 2019 IEEE Sustainable Power and Energy Conference (ISPEC). IEEE, pp. 699–703. https://doi.org/10.1109/iSPEC48194.2019.8975359.

Zhang, G., Li, Q., Chen, W., Meng, X., Deng, H., 2019a. A coupled power-voltage equilibrium strategy based on droop control for fuel cell/battery/supercapacitor hybrid tramway. Int. J. Hydrogen Energy 44, 19370–19383. https://doi.org/10.1016/j.ijhydene.2018.09.070.

Zhang, H., Yang, J., Zhang, J., Song, P., Li, M., 2020. Optimal energy management of a fuel cell-battery-supercapacitor-powered hybrid tramway using a multi-objective approach. Proc. Inst. Mech. Eng. - Part F J. Rail Rapid Transit 234, 511–523. https://doi.org/10.1177/0954409719849804.

Zhang, H., Yang, J., Zhang, J., Song, P., Xu, X., 2019b. A firefly algorithm optimization-based equivalent consumption minimization strategy for fuel cell hybrid light rail vehicle. Energies 12, 2665. https://doi.org/10.3390/en12142665.

Zhang, W., Li, J., Xu, L., Ouyang, M., 2017. Optimization for a fuel cell/battery/capacity tram with equivalent consumption minimization strategy. Energy Convers. Manag. 134, 59–69. https://doi.org/10.1016/j.enconman.2016.11.007.

Zhang, W., Li, J., Xu, L., Ouyang, M., Liu, Y., Han, Q., Li, K., 2016. Comparison study on life-cycle costs of different trams powered by fuel cell systems and others. Int. J. Hydrogen Energy 41, 16577–16591. https://doi.org/10.1016/j.ijhydene.2016.03.032.